The *Pyrococcus furiosus* ironome is dominated by [Fe₄S₄]²⁺ clusters or thioferrate-like iron depending on the availability of elemental sulfur

Shaik Waseem Vali¹, Dominik K. Haja², Richard A. Brand³, Michael W. W. Adams², and Paul A. Lindahl^{1,4}*

¹From the Department of Biochemistry and Biophysics, Texas A&M University, College Station, TX 77843 USA; ²Department of Biochemistry and Molecular Biology, University of Georgia, Athens, GA 30602 USA; ³Faculty of Physics, University of Duisburg-Essen, 47057 Duisburg, Germany and Institute of Nanotechnology, Karlsruhe Institute of Technology, 76344 Eggenstein-Leopoldshafen, Germany; ⁴Department of Chemistry, Texas A&M University, College Station, TX 77843-3255, USA

Running title: Pyrococcus furious ironome

*To whom corresponding should be addressed: Paul A. Lindahl, Department of Chemistry, Texas A&M University, College Station TX 77843-3255. Phone, 979-845-0956; Fax, 979-845-4719, email: lindahl@chem.tamu.edu.

Keywords: Mössbauer; Electron paramagnetic resonance; magnetically ordered; hyperthermophilic; archaea.

ABSTRACT

Pyrococcus furiosus is a hyperthermophilic anaerobic archaeon whose metabolism depends on whether elemental sulfur is $(+S^0)$ or is not (-S⁰) included in growth medium. Under $+S^0$ conditions, expression of respiratory hydrogenase declines while respiratory membrane-bound sulfane reductase and the putative iron-storage protein IssA increase. Our objective was to investigate the iron content of wild-type (WT) and ΔIssA cells under these growth conditions using Mössbauer spectroscopy. WT-S⁰ cells contained ~ 1 mM Fe, with \sim 85% present as two spectroscopically distinct forms of S = 0 [Fe₄S₄]²⁺ clusters; the remainder was mainly high-spin Fe^{II}. WT+S⁰ cells contained 5–9 mM Fe, with 75-90% present as magnetically ordered thioferrate-like (TFL) iron nanoparticles. TFL iron was similar to chemically-defined thioferrates; both consisted of Fe^{III} ions coordinated by an S4 environment, and both

exhibited strong coupling between particles causing high applied fields to have little spectral effect. At high temperatures with hyperfine interactions abolished, TFL iron exhibited two doublets overlapping those of $[Fe_4S_4]^{2+}$ clusters in $-S^0$ cells. This coincidence arose because of similar coordination environments of TFL iron and cluster iron. The TFL structure was more heterogeneous in the presence of IssA. Presented data suggest that IssA may coordinate insoluble iron sulfides as TFL iron, formed as a byproduct of anaerobic respiration sulfur under high conditions, which thereby reduces its toxicity to the cell. This was the first Mössbauer characterization of the iron-ome of an archaeon, and it illustrates differences relative to the iron content of better-studied bacteria such as Escherichia coli.

Pyrococcus furiosus is a hyperthermophilic anaerobic archaeon that grows near marine volcanic vents at temperatures approaching 100 °C (1). These cells grow on carbohydrates or peptides and produce acetate, CO₂, and either H₂ or H₂S depending on whether elemental sulfur (S⁰) is included in the growth medium. The iron concentration in the organism is high; this d-block transition metal plays critical roles in the cell's metabolism, especially in processes involving redox and energy generation (2). Bioinformatic analysis predicts that there are 178 iron-containing proteins (Table S1, (3), 27 of which have been purified (Table S2); at least 15 of those purified contain [Fe₄S₄] clusters. This represents 8.4% of the P. furiosus genome, which is slightly above average for archaea (7.1%) and well above average for bacteria (3.9%) eukaryotes (1.1%) (4, 5).

During peptide fermentation, homodimeric aldehyde ferredoxin oxidoreductase (AOR) oxidizes aldehydes derived from amino acids. Each AOR subunit contains an [Fe₄S₄] cluster. Bridging the subunits of the homodimer is a monomeric Fe ion coordinated by His and Glu residues (6). AOR constitutes ~ 1% of the total protein in the cell (7). Formaldehyde ferredoxin oxidoreductase (FOR), pyruvate ferredoxin oxidoreductase (POR), ketoisovalerate ferredoxin oxidoreductase 2-ketoglutarate (VOR), ferredoxin oxidoreductase (KGOR), and indolepyruvate ferredoxin oxidoreductase (IOR) are all [Fe₄S₄] cluster-containing enzymes that catalyze catabolic processes. The latter enzymes catalyze the oxidative decarboxylation of 2keto acids derived from peptides (8,9,10). Electrons from these catabolic metalloenzymes reduce a monomeric ferredoxin that houses a single $[\text{Fe}_4\text{S}_4]^{2+/1+}$ cluster $(\text{E}^0, \sim -480 \text{ mV vs})$ NHE) coordinated by 3 Cys and 1 Asp residues. fermentation Carbohydrate involves modified Embden-Meyerhof pathway that is independent of NAD. Glyceraldehyde-3oxidoreductase phosphate ferredoxin

(GAPOR), another [Fe₄S₄]-containing enzyme, oxidizes glyceraldehyde-3-phosphate to glycerate-3-phosphate and transfers the electrons obtained to the ferredoxin.

Ferredoxin not only receives electrons but it donates them as part of energy generation in the cell; thus, it serves as the electron currency for the cell. An evolutionarily ancient membranebound respiratory hydrogenase (MBH) is used to oxidize ferredoxin (11). This contains at least three [Fe₄S₄] clusters and a NiFe activesite cluster. Ferredoxin donates electrons to MBH which transfers them, in turn, to protons (E^0) = -420 mV at pH 7), forming H₂ as the product. This thermodynamically favorable redox process pumps H⁺ ions across the membrane, which are then exchanged with Na⁺ ions. This creates a concentration gradient that is used by a Na+-dependent ATP synthase to generate ATP via chemiosmosis. Ferredoxin also donates electrons to NADH-dependent reduced ferredoxin:NADP+ oxidoreductase 1 (Nfn1) which reduces NADP⁺ in an electron bifurcation reaction that generates lowpotential electrons which can be used in metabolic processes requiring low potentials.

Carbohydrate fermentation can occur with or without S⁰, whereas cells grown on peptides require S⁰ as there is little growth when it is omitted from the growth medium (12). The metabolism of *P. furiosus* changes significantly when elemental sulfur (S⁰) is included in the growth medium (13). Under $+S^0$ conditions, P. furiosus shuts-down expression of MBH and of NAD(P)-reducing soluble two hydrogenases termed SHI and SHII (among other proteins) and up-regulates expression of a membrane-bound sulfane reductase (MBS) (Tables S3 and S4 (14)). Doing so suppresses production of H₂ and stimulates H₂S production. MBS uses electrons ferredoxin to reduce sulfane sulfurs of polysulfides (E^{0} ' = -260 mV), generating smaller polysulfide units as illustrated by the following sample reaction.

$$\overline{\ }: \overset{\cdot}{\mathbf{S}} - \overset{\cdot}{\mathbf{S}} - \overset{\cdot}{\mathbf{S}} - \overset{\cdot}{\mathbf{S}} = \overset{\cdot}{\mathbf{S}} : \overline{\ } + 2e^{-} \longrightarrow \overline{\ }: \overset{\cdot}{\mathbf{S}} - \overset{\cdot}{\mathbf{S}} : \overline{\ } + \overline{\ }: \overset{\cdot}{\mathbf{S}} - \overset{\cdot}{\mathbf{S}} : \overline{\ }$$

MBS cleaves organic and anionic polysulfides but not to the level of H_2S , which is formed spontaneously from smaller polysulfides (S_n^{2-}) where $n \le 4$. Like MBH, MBS creates a Na^+ ion gradient which is subsequently used, *via* chemiosmosis, for ATP synthesis. MBS is a homolog of MBH and also contains three $[Fe_4S_4]$ clusters. Unlike MBH, it does not contain a NiFe active site (15).

The S⁰-dependent shift in metabolism is controlled by transcription factor SurR (16,17). Under +S⁰ conditions, SurR upregulates iron transport and ISC biosynthesis genes. *P. furiosus* grows better with S^o than without it; in fact, the maximal yield (cell mass produced per mole of carbohydrate used) is nearly double that obtained in the absence of S^o (herein termed -S⁰). This implies that more energy can be generated by coupling ferredoxin oxidation to S^o reduction than by coupling it to proton reduction, a conclusion substantiated by the finding that MBS contains an additional ion pump compared to MBH (15).

Despite being an anaerobe, *P. furiosus* houses iron-containing proteins that protect it against damage due to reactive oxygen species (ROS). Superoxide reductase catalyzes the reduction of superoxide to H₂O₂ at an active site containing a single Fe^{II} ion. The electrons required for this come from rubredoxin, a protein that houses a mononuclear redox-active Fe^{II}/Fe^{III} ion coordinated by four cysteine residues in a tetrahedral geometry – an Fe^{II/III}(S)₄ site (18). Rubrerythrin catalyzes the reduction of H₂O₂ to water, also using electrons from rubredoxin. It contains an [Fe-O-Fe] center as well as an Fe^{II/III}(S)₄ site (19).

P. furiosus contains at least two proteins that store iron, including ferritin and a "miniferritin" DPS-like protein. Ferritin stores thousands of ferric ions within the core of a 24-subunit protein complex as an insoluble Fe^{III} ferrihydrite-type aggregate. The DPS-like protein has a ferroxidase active site ([Fe-O-Fe])

which exhibits peroxidase activity in the presence of H_2O_2 . This protein coordinates hundreds of iron ions, obtained from the H_2O_2 -dependent oxidation of Fe^{II} (20,21).

Another protein that binds a large amount of iron is IssA. The exact function of the IssA protein is unknown but its expression increases dramatically when cells are grown in $+S^0$ media, but only when iron is present ($> 7.4 \mu M$) (22). Vaccaro et al. (23) suggested that IssA stores iron as thioferrates in which Fe^{III} and S²ions form anionic chains of edge-sharing FeS₄ tetrahedra that are charge-neutralized by cations such as Na⁺ or K⁺. Using TEM, they detected iron-dense particles 20 - 300 nm in diameter in $+S^0$ P. furiosus cells (23). X-ray absorption spectra of the particles indicate a linear polymeric (FeS2⁻)_n structure as in this includes thioferrates: four interactions at 2.24 Å, two Fe-Fe interactions at 2.70 Å, and a long-range Fe-Fe interaction at 5.4 Å. The particles exhibit a broad isotropic EPR signal at g = 2.2 that displays anti-Curie Law behavior, also consistent with thioferrates. The EPR signal is observed only above 60 K. similar to the behavior of synthetic thioferrates. Moreover, the iron and sulfur from IssAassociated particles assemble into [Fe₄S₄] clusters. Such clusters can transfer to apoferredoxin (in the presence of DTT), indicating that these thioferrate particles can be used in ISC assembly. Purified IssA monomers reportedly contain 38 Fe and 38 S atoms. A 20 nm diameter 3.5 MDa thioferrate structure is calculated to contain ~ 6400 Fe atoms and ~ 170 IssA monomers. IssA contains only 1 cysteine per monomer raising issues as to how it coordinates such structures.

In this study, we have used primarily Mössbauer (MB) spectroscopy to analyze the iron content of 57 Fe-enriched WT and IssA Δ whole *P. furiosus* cells grown on the disaccharide maltose in the presence (+S 0) and absence (-S 0) of elemental sulfur. All 57 Fe ions in a sample are detectable by MB spectroscopy, with intensities that are roughly invariant per

iron in the sample, regardless of the type of iron center. Thus, MB can be used to evaluate the ironome of these cells, albeit in semiquantitative terms and only with "coarse-grain" resolution. Using this approach, we have previously evaluated the ironome Escherichia (24),Saccharomyces coli cerevisiae (25), and human Jurkat cells (26). This is the first MB study of an archaeon, in this case one that is hyperthermophilic and strictly anaerobic.

Results

WT-S⁰ cells harvested while growing exponentially: We began by collecting lowtemperature low-field MB spectra of whole WT cells harvested while growing exponentially on maltose with 10 µM ⁵⁷Fe and without S⁰ in the medium. The 5 K 0.05 T MB dominated by a broad spectrum was quadrupole doublet representing ca. 85% of the overall intensity (Figure 1A). The structured lineshape of the doublet prompted us to decompose it into two partially-resolved sharper doublets, each with isomer shifts δ typical of oxidized S = 0 [Fe₄S₄]²⁺ clusters (Table 1). The doublets were simulated by the gold and brown solid lines of Figure 1. The quadrupole splitting ΔE_0 associated with the gold doublet was wider than that of the brown doublet, and so we labeled them wide and narrow iron sulfur cluster doublets (ISCw and ISC_N). Each doublet represented 35% - 45% of spectral intensity; the exact percentage due to each was difficult to assess because they were not well resolved. Considering that the spectrum represented all irons in the cell, including at least 15 different [Fe₄S₄]containing proteins (Table S2), the ability to decompose all [Fe₄S₄] clusters into two doublets, each with relatively sharp linewidths, was remarkable. One extreme explanation was that 2 of the 15 [Fe₄S₄]-containing proteins in the cell dominated the iron content of the cell. with each protein corresponding to the two doublets. At the other extreme, each [Fe₄S₄]-

containing proteins in the cell might have contributed equally to the spectrum but, for some unknown reason, segregated cleanly into these two spectral groups. Neither extreme seems likely but they illustrate the remarkability of the result.

[[Insert Figure 1 and Table 1]]

Also remarkable was that δ and ΔE_Q for the two doublets were strongly temperature-dependent. At 150 K (Figure 1B), ΔE_Q and δ for both doublets declined (Table 1) but their linewidths did not increase. The temperature dependence of δ is mostly related to the second-order Doppler effect (27). The temperature-dependence of ΔE_Q is generally attributed to changes in the covalency of metalligand bonds. This can bring the separation between t_{2g} and e_g atomic orbitals close enough together that orbital populations can be affected by temperature, changing ΔE_Q .

Continuing with the extreme explanations offered above, this result would mean either that both dominant [Fe₄S₄] proteins exhibited this behavior, or that all 15 contributing [Fe₄S₄] proteins did so. This raises an intriguing speculation that [Fe₄S₄]²⁺ clusters in hyperthermophilic organisms might generally possess low-lying excited states.

We wanted to determine whether these doublets arose from diamagnetic iron centers, as would be the case if they arose from [Fe₄S₄]²⁺ clusters. Spectra were collected at 4.2 K and 0, 3, and 6 T applied magnetic fields (Figure 1, C - E). The solid red lines overlaying the data were simulations that assumed diamagnetism and the δ and ΔE_0 values in Table 1. The reasonable fits demonstrated that the $ISC_{W/N}$ doublets indeed arose from S = 0 $[Fe_4S_4]^{2+}$ clusters. This conclusion was reinforced by the large number of [Fe₄S₄]containing proteins in these cell (Table S2). These spectra also show that virtually all redox-active [Fe₄S₄] clusters in exponentially growing WT-S⁰ cells are in the oxidized 2+

core state. $[Fe_4S_4]^{2+/1+}$ clusters typically have reduction potentials of ca. -400 mV vs. NHE, suggesting (by considering the Nernst equation) a cellular potential > ca. -340 mV.

After MB spectra were collected, the sample was thawed and, after EPR analysis (see below), the metal content was determined (Table S5). We assumed that 70% of the sample volume in the packed MB cup was due to the cells themselves and that the density of the sample was 1.00 g/ml. With these assumptions, we calculated that the sample contained 1.03 mM iron. If 2 [Fe4S4]-containing proteins dominated this group, their cellular protein concentrations would be $\sim 120~\mu M$ each. On the other hand, if all 15 [Fe4S4] proteins contributed equally, their the average cellular concentration would be $\sim 17~\mu M$ which seems more likely.

WT-S⁰ cells exhibited broad unresolved intensity barely distinguishable from the baseline between ca. -5 and +6 mm/s (Figure 1A, arrows). This feature represented roughly 15% of the overall intensity and appeared to arise from a paramagnetic iron center. We overlaid the S⁰-dependent thioferrate-like (TFL) magnetic material described below onto it, but the mismatch suggested a different type of magnetic iron (called "other magnetic iron" in Table 1). By 150 K, the associated magnetic hyperfine interactions collapsed completely into the spectral region occupied by the ISCw/N doublets (Figure 1B). Importantly, we are not concluding that the absorption necessarily collapsed into the ISCw/N doublets at high temperature, only that it occupied/overlapped the same spectral region; more on this distinction below.

A small amount of a high-spin Fe^{II} doublet (~5%) was also evident in the 150 K spectrum of WT-S⁰ cells (Figure 1B, double arrow). A similar doublet was probably present in the 5 K spectrum (Figure 1A), but it could not be distinguished from the "other magnetic" iron. The parameters associated with this doublet are typical of mononuclear and binuclear Fe^{II} sites

in proteins with 5-6 O/N donor atoms (Table S2), as well as any low-molecular-mass Fe^{II} species with a similar ligand environment. There are few if any sulfur donors in the $Fe^{II}(O/N)_{5-6}$ sites. Given the overall iron concentration in the cell, this doublet represented $\sim 50~\mu M$ $Fe^{II}(O/N)_{5-6}$ total in *P. furiosus* cells.

The 4.2 K 0 T spectrum of WT-S⁰ cells in Figure 1C exhibited two minor features. One was a line at ~ 2.6 mm/s which reflected an Fe^{II}(O/N)₅₋₆ doublet. This doublet was simulated by the blue solid line above the spectrum at 15% intensity. The broad non-symmetrical shape of the high-energy line suggested at least two Fe^{II}(O/N)₅₋₆ sites. The second minor feature, simulated by the solid green line, was a pattern barely distinguishable from the baseline that suggested a high-spin Fe^{III} species. The putative S = 5/2 species was most evident at 6 T (Figure 1E) where it represented $\sim 15\%$ of overall spectral intensity.

[[Insert Fig. 2]]

The EPR spectrum of the sample (after thawing the MB sample and transferring it to an EPR tube) exhibited a signal at g = 4.3 which probably originated from the same species (Figure 2, bottom). It also exhibited an isotropic signal at g = 2.00 but little intensity at g = 1.94 which is consistent with MB spectra showing that the [Fe₄S₄] clusters in the cell were primarily in the diamagnetic 2+ core oxidation state.

The most surprising aspect of the Figure 1C spectrum was that the sample used to generate it was identical to that of Figure 1, A and B only that it had been stored without thawing in a liquid N_2 dewar for ~ 3 months. Since the ISC_{W/N} doublets were unaffected, iron species other that the clusters affording the ISC_{W/N} doublets (perhaps the "other magnetic" iron) must have reacted slowly in frozen cells to generate the observed high-spin Fe^{II} and Fe^{III} spectral features in Figure 1, C - E. The S = 5/2

Fe^{III} feature is probably an artefact as we have not observed similar features in other spectra. In contrast, Fe^{II}(O/N)₅₋₆ features were often observed under various conditions, and thus are likely physiologically relevant.

WT+S⁰ cells harvested while growing **exponentially:** Another batch of *P. furiosus* cells was grown in the same medium except under +S⁰ conditions. They were also harvested while growing exponentially. The lowtemperature low-field MB spectrum of the WT+S⁰ cells (Figure 3A) was dominated by broad absorption that extended from ca. -6 mm/s to +7 mm/s velocity. Given previous studies showing large quantities of TFL material in +S⁰ cells, we assigned it to this material. Consistent with that assignment, the EPR spectrum of cells in this state lacked a significant g = 4.3 signal (Figure 2, top indicating the absence spectrum), magnetically isolated high-spin S = 5/2 Fe^{III} paramagnetic material in the sample.

[[Insert Fig. 3]]

The spectrum exhibited two strong absorption lines in the same region of the ISCw/N doublets in WT-S⁰ spectra, and this unfortunately created ambiguity for our analysis. It implies that some proportion of the intensity of these two lines arose from the ISCw/N doublets while the remainder was associated with the TFL material. Based on our simulations and analyses, we estimate that at least 10% and no more than 25% of the spectral intensity arose from the ISC_{W/N} doublets in WT+S⁰ spectra. The relative intensity of the two contributions was kept constant in the 3.0 and 6.0 T spectra (Figure 3, C and D) with 20% of the intensity attributed to the ISC_{W/N} doublets in the 6.0 T spectrum. The solid green lines in Figure 3, A, C, and D simulated the ISCw/N doublets at the 20% intensity level.

Magnetic hyperfine interactions associated with the TFL material were absent in the WT+S⁰ spectrum at 150 K (Figure 3B), and the

intensity associated with this material collapsed into the same region that was occupied by the ISCw/N doublets in WT-S 0 spectra. The intensity of the ISCw doublet increased from $\sim 10\%$ at 5 K to 33% at 150 K. The intensity of ISCN increased from $\sim 10\%$ at 5 K to 65% at 150 K. Thus, 30% of the TFL material collapsed over the ISCw doublet while 70% collapsed over the ISCN doublet. None of the TFL material collapsed into features characteristic of Fe^{II} ions.

The 150 K MB spectrum of the WT+S⁰ sample did exhibit a minor broad Fe^{II}(O/N)₅₋₆ doublet, representing ~ 4% of spectral intensity (Figure 3B, arrow). This doublet required two species for fitting, using parameters of mononuclear Fe^{II} species coordinated by 5-6 O/N and no S ligands (Table 1). These Fe^{II}(O/N)₅₋₆ sites are independent of the TFL material but became apparent once the hyperfine interactions associated with the TFL material collapsed.

We were initially surprised that the TFL magnetic material in WT+S⁰ cells had isomer shift and quadrupole splitting parameters (56% $\delta = 0.37$ mm/s and $\Delta E_0 = 0.75$ mm/s; 44% $\delta =$ 0.42 mm/s and $\Delta E_0 = 1.15 \text{ mm/s}$) that were indistinguishable from those due to the S = 0[Fe₄S₄]²⁺ clusters in the WT-S⁰ cells, given that the low-temperature magnetic properties of the two types of iron species were entirely different. This coincidence probably arose because the local structures of the two types of iron species were remarkably similar. Authentic sodium thioferrate (NaFeS₂) exhibits $\delta = 0.36$ mm/s and $\Delta E_Q = 0.58$ mm/s (28), which are similar to those of the TFL material AND [Fe₄S₄]²⁺ clusters in these cells. Thioferrates consist of anionic linear chains of ((Fe^{III}S₂)⁻)_n units, with each Fe^{III} ion coordinated by a tetrahedral environment of sulfide ligands with Na⁺ or K⁺ counter ions. Likewise, each iron of [Fe₄S₄] clusters are locally coordinated by four sulfur ligands in a tetrahedral environment. The average formal oxidation state of iron in [Fe₄S₄]²⁺ clusters is

+2.5, with one delocalized electron shared by two irons in a "mixed-valence" [Fe^{II} Fe^{III}] pair (the two pairs of a cluster are then antiferromagnetically coupled to generate the S = 0 system spin). There were clearly no localized Fe^{II}(S)₄ sites with sulfur donor sites in the TFL material, since otherwise an intense quadrupole doublet with $\delta \sim 0.7$ mm/s and $\Delta E_Q \sim 3$ mm/s (similar to reduced rubredoxin) would have been observed in the 150 K spectrum of Figure 3B. On the other hand, some *delocalized* [Fe^{II} Fe^{III}] units might have contributed to the TFL structure.

We had hoped that high-field spectra of the WT+S⁰ sample would have been sufficient to break the magnetic coupling responsible for the broadness and poor resolution of the magnetic material in low fields, but this was not observed. The spectra at 4.2 K and 0, 3, and 6 T perpendicular applied fields included contributions from both the magnetically-ordered iron and ISCs (Figure 3, A, C and D). The ISC contribution was calculated as described in *Experimental Procedures*. The known external field and isomer shift were used to calculate the ISC portion of the spectrum so that in the fitting interaction only the area of this contribution was varied.

Technical Details regarding the physical properties of the TFL material in WT+S⁰ cells: The following technical aspects can be skipped without losing the major conclusion that the thioferrates-like material is similar to authentic thioferrates but with some subtle differences. This section provides details of those differences.

The magnetic part of the spectra (Figure 3A, C and D in red) was modelled with a histogram of hyperfine sextets over a range of effective hyperfine fields in steps of 1 T. The resulting histograms are presented in Figure 3 E, F and G. Small variations in δ and quadrupole line shift 2ϵ have been used to approximate the spectral asymmetry of the magnetic part. 2ϵ is similar to ΔE_Q but it includes an angular

dependence, even when the general asymmetry parameter that is absent in ΔE_Q , $\eta = 0$ (27).

These were assumed linear in the effective hyperfine field over the fitted range. The intensities of each sextet were then used to calculate the distribution $P(B_{hf})$. The angle Θ of the hyperfine field B_{hf} with respect to the gamma radiation determines the line intensity ratio A_{23} between line pair 2 and 5 (nuclear transition with $\Delta m = 0$) to 3 and 4 (transitions with $\Delta m = \pm 1$), which can vary between 0 (for $\Theta = 0$; moments parallel to the gamma ray) and 4 (for $\Theta = 90^{\circ}$) according to the equation

$$A_{23} = \frac{4\sin^2\Theta}{1+\cos^2\Theta}$$

(27). An isotropic distribution of directions yields a ratio of 2, similar to what was observed (Figure 4). In these experiments, the external magnetic field was perpendicular to the gamma rays. Thus, we can assume rotational symmetry around the field but not around the gamma ray direction. Useful relations for simple cases of magnetic texture have been described (29, 30).

[[Insert Fig. 4]]

Several changes are expected when a magnetic field is applied to a magnetically ordered system. First for a ferromagnet or ferrimagnet, the magnetic moments should align parallel to the field. An antiferromagnet will align perpendicular to the field as long as the crystalline anisotropy is not too large. Since the orbital component of the Fe^{III} ions moments is zero (with the ground state configuration [Ar]3d⁵ having L=0, S=5/2), the crystalline anisotropy is small compared to Fe^{II} (with [Ar]3d⁶ and L=2, S=2). Then depending on orientation, the external field would add vectorially to the local hyperfine field (which for Fe^{III} is antiparallel to the local moment). If, as we shall see below, moments do not realign in a large magnetic field, either the crystalline anisotropy is large (for example with Fe^{II}) or the magnetic interactions are frustrated. Frustration can be caused by competing

exchange interactions that cannot all be satisfied, leading to complicated magnetic ground states (31). A Gaussian distribution was assumed for the remaining magnetic part as described by the average value $\langle B_{hf} \rangle$ and standard deviation σ . We also simulated the spectra with an unconstrained histogram distribution and the results were similar though the overall distributions were somewhat more variable from one spectrum to the next.

The indicated effective hyperfine field (Figure 3, right side) was the vector sum of the true local hyperfine field and the external field. The area of the ISC_{W/N} contribution (green line) was varied to minimize χ^2 error-residuals. The ISC_{W/N} doublets represented 20% of the overall intensity. The calculated distributions of hyperfine fields for all three spectra were centered at $\langle B_{hf} \rangle \sim 24$ T with a Gaussian standard deviation of $\sigma = 6$ T. The distribution was essentially invariant up to a 6 T applied field. In addition, the relative intensities of lines 2 (and 5) with respect to lines 3 (and 4) did not change with applied fields, staying essentially equal to 2 up until at least 6 T (Figure 4). This indicates that the magnetic system is remarkably rigid. In the case of Fe^{III}, this rigidity is unlikely to be due to crystalline anisotropy. A more likely explanation is that it arises from the frustration of the magnetic exchange interactions. Such processes are known for systems with antiferromagnetic interactions dominated by site-disorder or triangular lattices. In the current case, it seems more likely that the origin of the frustration is antiferromagnetic interactions disorder, similar to the properties of canonical spin glasses (31),or a disordered superparamagnetic material below the blocking temperature T_{BK}.

In contrast, the equivalent high-field low-temperature spectra of thioferrates exhibits a well-resolved six-line pattern (32). A similar six-line pattern is also observed for thioferrates in spectra collected at zero or low applied field. Thus, the magnetically ordered material in *P*.

furious, obtained in WT+S⁰ cells, does not have exactly the same magnetic properties as synthetic Na⁺/K⁺ thioferrates even though the high-temperature MB parameters are similar.

Superparamagnetic materials exhibit anti-Curie Law behavior and can be characterized by its T_{BK}. T_{BK} is operationally defined as the temperature at which half of the spectral hyperfine intensity exhibits magnetic interactions and half is collapsed into quadrupole doublets. To determine this for the TFL magnetic material in P. furiosus, we collected spectra at various temperatures (Figure 5). Temperatures as high as ca. 135 K were required for all magnetic material to collapse into doublets; from this we estimated $T_{BK} \approx 40 - 50 \text{ K}$. In contrast, all magnetic material in spectra of synthetic thioferrates is collapsed between 4.2 K and 77 K (28), implying a slightly lower T_{BK}. This is another indication that the magnetic properties of the TFL material in P. furiosus differed in subtle ways from synthetic thioferrates.

To summarize these technical comments, the TFL material exhibits some magnetic properties that are similar to authentic thioferrates, but there are some physical/spectroscopic differences. We are unable to interpret these differences in an unambiguous manner to propose a chemically-defined structure for this novel material, so we can only conclude that it is thioferrate-*like*.

[[Insert Fig. 5]]

After collecting these spectra, the sample was thawed and the metal contents determined (Table S5). The iron concentration in the WT+S⁰ sample was 5.25 mM – about 5-fold higher than the WT-S⁰ sample. Most or all of this additional iron was due to the TFL iron described above. If the expression levels of the [Fe₄S₄]-containing proteins were unchanged with the added sulfur, ca. 20% of the spectral intensity should have been ISC_{W/N} doublets. This is within our estimate of 10% - 20%. Our data (weakly) support a slight decline in the

expression levels of the [Fe₄S₄]-containing proteins when S⁰ is included in the medium. Also noteworthy is that WT+S⁰ cells contained significantly higher concentrations of Cu, Mn, and Zn than WT-S⁰ cells (Table S5) indicating a widespread S⁰-dependent shift in metal-associated processes.

WT Cells harvested in stationary state: We next collected MB spectra of WT cells grown as above, with and without S⁰, but harvested at stationary state. Both 5 K and 150 K MB spectra of WT-S⁰ cells (Figure 6, A and B) were dominated by ISC_{W/N} doublets that collectively accounted for ca. 75% of spectral intensity. Also evident were overlapping doublets due to at least two types of Fe^{II}(O/N)₅₋₆ species. Their collective intensity was ca. 23%, significantly greater than for samples harvested during exponential growth. No magnetic material was evident and the only intense feature in the corresponding EPR spectrum was an isotropic signal at g = 2.00.

A minor Fe^{II}(S)₄ species was evident in the 150 K spectrum (Figure 6B), as indicated by the arrow which highlights the low-energy line of the corresponding doublet. The solid green line simulates this species using parameters in Table 1. The doublet represented only ~2% of spectral intensity but we observed it in multiple spectra. Such doublets are typical of Fe^{II} ions coordinated by a tetrahedral environment of sulfur donors. *P. furiosus* contains 2 proteins with such Fe^{II}(S)₄ sites, rubredoxin and rubrerythrin (Table S3).

[[Insert Fig. 6]]

The 5 K spectrum of WT+S 0 stationary state cells (Figure 6C) was similar to that of exponentially growing WT+S 0 cells in that it was dominated by a broad feature spanning from -6 mm/s to +7 mm/s. This feature was assigned to the TFL material. Two intense lines near the center of the spectrum had parameters of ISC_{W/N} doublets; they collectively represented no more than $\sim 25\%$ of spectral

intensity as some portion of this was due to TFL material (Figure 6C).

magnetic hyperfine The interactions associated with the TFL material were abolished at 150 K (Figure 6D), with the intensity from this material collapsing over the ISC_{W/N} doublets. As was observed with hightemperature spectra of exponentially grown cells, the ISC_N doublet became relatively more intense than the ISCw doublet indicating that the TFL magnetic material collapsed mainly over the ISC_N doublet. A broad Fe^{II}(O/N)₅₋₆ doublet was also evident in the 150 K spectrum (arrow in Figure 6D). Its intensity ($\sim 4\%$) was similar for the WT+S⁰ sample harvested under exponential conditions but less than for the WT-S⁰ sample harvested in stationary state.

After these spectra were collected, samples were thawed and analyzed for metal content. The iron concentrations in WT-S⁰ and WT+S⁰ cells were 660 μ M and 8700 μ M, respectively (Table S5). If the average expression level of [Fe₄S₄]-containing proteins remained unchanged with the addition of elemental sulfur, ~ 7% of the spectral intensity of Figures 6, C and D would be due to ISC_{W/N}. Our fitting analysis suggests slightly higher percentage range, namely 10% - 25%.

ΔIssA cells: The gene encoding the IssA protein is highly expressed under +S⁰ conditions and IssA is thought to be intimately involved in forming TFL nanoparticles. To investigate this further, we grew cells that lacked the gene encoding this protein, the ΔIssA strain, to determine whether it could form TFL iron. We first grew the deletion strain on the same medium as for WT-S⁰ cells, and harvested cells during exponential growth as a control. Their 10 K 0.05 T MB spectrum (Figure 7A) was dominated by the ISCw/N doublets (~80% total). The spectrum also exhibited a broad doublet due to at least 2 Fe^{II}(O/N)₅₋₆ species, representing 12% of the overall intensity (double arrows on the right), and to a minor Fe^{II}(S)₄ doublet representing ~

3% of the intensity (single arrows). The 150 K spectrum (Figure 7B) exhibited the same features, with the temperature-dependence of the ISC_{W/N} doublets visually apparent and both Fe^{II} doublets better resolved. The 4.2 K 6.0 T spectrum (Figure 7C) was simulated assuming that the ISC_{W/N} doublets were diamagnetic, confirming that they arose from S = 0 [Fe₄S₄]²⁺ clusters.

[[Insert Fig. 7]]

ΔIssA+S⁰ cells were grown and harvested similarly. Their low-temperature MB spectra exhibited an intense six-line spectra at all applied fields (Figure 8, A - C). Most or all of the spectral intensity arose from the TFL material. The peaks were better resolved than the corresponding spectral features in the $WT+S^0$ spectra, implying some IssAdependent structural differences. Surprisingly, the positions of the lines were unaffected by applied fields as high as 6.0 T, though the linewidths broadened with increasing field. This implied that the magnetic coupling between particles in the material was significantly stronger than the applied fields and could not be broken at 6 T.

[[Insert Fig. 8]]

Technical Details regarding the Physical properties of the TFL material in $\Delta IssA+S^0$ cells: Again, the following are technical details that can be skipped without loss of continuity. There were several differences in the magnetism of the $\Delta IssA+S^0$ sample compared to the WT+S⁰ exponential sample. Specifically, the extent of broadening of the distribution with external field was greater, and there was a gradual change in the relative line intensity A_{23} (Figure 4).

Antiferromagnets orient perpendicular to an external field when the crystalline anisotropy is not excessive. In that case all moments would be in a plane that includes the gamma rays. Kuncser et al. (29,30) has given several

expressions for A_{23} in different cases. Using their result for moments in a plane with the gamma ray (see Ref 30, Eq. 7'), we obtain $A_{23} = 4/3 = 1.33$, which is about what is observed for an external field of 6 T. Thus, the interactions appear to be strongly antiferromagnetic but with less crystalline anisotropy or frustration than in the WT+S⁰ exponential sample.

We also collected low-field spectra at increasing temperatures (Figure 9) to observe the loss of magnetic hyperfine interactions. Both with Gaussian and Histogram models were fitted to the spectra. Average results for the two methods (average Bhf, width of the distribution P(Bhf)) were similar. Fits assuming the Gaussian model broadened dramatically at 55 K, caused by a strong increase of a low field component. T_{BK} was ~ 50 K, similar to that obtained for the TFL nanoparticles in WT+S⁰ cells. Determining the magnetic component for temperatures above 55 K was difficult due to components. overlap with the ISC_{W/N} However, the transition with increasing temperatures was similar to superparamagnetism observed in fine grains (33). The linewidths for ISC_{W/N} components remained remarkably sharp with increasing temperatures (Table 1).

[[Insert Fig. 9]]

In summary, these technical details describe how the TFL nanoparticles in $\Delta IssA+S^0$ cells are somewhat different from those in WT+S⁰ cells. Again, we are unable to interpret those differences in unambiguous chemical/structural terms apart from concluding that the material is more crystalline/homogenous in the absence of IssA.

After spectra were collected, the sample were thawed and cellular metal and overall protein concentrations were determined; the protein concentrations in $\Delta IssA-S^0$ and $\Delta IssA-S^0$ samples were 78 ± 3 mg/ml and 36 ± 2 mg/ml, respectively. Metal concentrations are in Table S5.

Growth Experiments: Two roles have been proposed for IssA; that it is involved in Fe storage, or that it serves to detoxify insoluble FeS clusters (22,23). In order to test the role of IssA in Fe storage, WT cells were harvested after growth under $+S^0$ and $-S^0$ conditions, and $\Delta IssA$ under $+S^0$ conditions. The harvested cells were washed and used to inoculate irondepleted medium; if IssA binding of TFL increase aggregates serves to the bioavailability of the iron, only WT+S⁰ cells should have grown in this iron-depleted medium. However, there was no growth in any of the iron-depleted medium, no matter what cells were used to inoculate the medium (data not shown).

[[Insert Fig. 9]]

To test whether IssA is used to detoxify insoluble Fe/S aggregates, WT and ΔIssA strains were grown with and without adding 50 µM iron in both 10 mM sodium sulfide medium (low IssA expression, Figure 10A) and 1 g/l S^0 medium (High IssA expression, Figure 10B). Under low sulfide concentrations, all strains similarly high grew to cell protein concentrations in culture (~90 $\mu g/ml$), suggesting that high iron concentrations by themselves are not toxic to the cell. On the other hand, under + S⁰ (high sulfide) conditions, increasing the Fe concentration led to a significant decrease in growth in both WT and $\Delta IssA$ strains. Additionally, the $\Delta IssA$ strain only reached half the cell protein concentration as WT under normal (10 µM) Fe conditions, suggesting that IssA sequesters iron, in the presence of sulfur, that would otherwise be toxic.

Discussion

Our results demonstrate that the iron content or ironome of *P. furiosus* cells changes dramatically when elemental sulfur is added to the growth medium. Under -S⁰ conditions, most of the iron in the cell is S = 0 [Fe₄S₄]²⁺

clusters. Under +S⁰ conditions, the cell imports ~ 5 times more iron, with 75-90% eventually forming TFL aggregates. Some of the iron in WT+S⁰ cells must have been in the form of [Fe₄S₄]²⁺ clusters, but quantifying how much was in this form proved difficult because the MB spectral features of TFL iron were indistinguishable from those of [Fe₄S₄]²⁺ clusters at high temperatures, and at low temperatures, the contribution of diamagnetic [Fe₄S₄]²⁺ clusters was obscured by the dominating magnetic features of the TFL aggregates. Simulations of the low-temperature spectral pattern of the $\Delta IssA+S^0$ cells indicated that the [Fe₄S₄] contribution was negligible. All things considered, we tentatively conclude that the overall expression level of [Fe₄S₄]containing proteins decreases somewhat under +S⁰ conditions. This supports a shift in cellular metabolism when elemental sulfur is present. [Fe4S4]-containing hydrogenases are downregulated under $+S^0$ conditions (13), and cells grow faster under +S⁰ conditions as long as sufficient iron is included in the growth media. We also found that concentrations of other metals (Cu, Mn, Zn) were significantly higher in cells grown under +S⁰ conditions, again indicating major metal-associated metabolic changes.

We characterized the TFL iron in $+S^0$ cells. This material is closely related to authentic thioferrates in that both synthetic thioferrates and the TFL iron consist predominantly of Fe^{III} ions coordinated to four sulfide ions in a tetrahedral geometry. Neither form of iron contains *localized* Fe^{II}(S)4 units, but we cannot exclude the possibility that TFL iron includes some *delocalized* [Fe^{II} Fe^{III}] units. This situation is found in [Fe₄S₄] clusters which have virtually the same δ and Δ E_Q values as TFL iron.

At low temperatures, authentic sodium thioferrate (NaFeS₂) exhibits a well-resolved sextet including magnetic hyperfine interactions of magnitude 270 kG (28). This hyperfine field is unusually small for ferric ions

due to a high degree of covalency with sulfur. Using MB spectroscopy, Zink and Kargony (32) examined authentic KFeS₂ at variable applied perpendicular fields up to 5 T. At all applied fields, synthetic thioferrates displayed a sextet that was not strongly affected by the field. Similarly, the TFL material in both WT+S⁰ and $\Delta IssA+S^0$ cells was not strongly affected by applied fields up to 6 T. This suggests even stronger interactions in TFL iron than in synthetic thioferrates. The spectra again show line-splittings characteristic of magnetic ordering including line broadening typical of a continuous distribution of hyperfine fields. $\Delta IssA+S^0$ spectra were analyzed assuming no ISC contribution.

One of the most surprising conclusions from this work is that the IssA protein is NOT required for forming TFL particles as these particles formed in *P. furiosus* cells lacking IssA. In fact, the spectral properties of TFL particles in the absence of this protein were closer to synthetic thioferrates as they exhibited a well-resolved six-line pattern at 5 K. The poorer spectral resolution associated with the TFL material in WT+S⁰ cells may be due to a more heterogeneous distribution of TFL structures. We considered that IssA disrupts the thioferrate structure, perhaps making the material more bioavailable to the cell, but it does not appear to do so.

also examined We the temperaturedependence of hyperfine interactions, and used both Gaussian and Histogram models to fit the spectra. Average results for the two methods (average <Bhf>, width of the distribution P(Bhf)) were similar. Fits assuming the Gaussian model broadened dramatically at 55 K, caused by a strong increase of a low-field component. Determining this component for temperatures above 55 K was made difficult by the overlap with the ISC_{W/N} components. However, the transition with increasing temperatures was similar to the superparamagnetism of fine grains (33).

By 77 K, these interactions are fully abolished in synthetic thioferrates whereas some interactions remained at this temperature in the P. furiosus TFL aggregates. T_{BK} of the TFL material is thus slightly higher than for authentic thioferrates. T_{BK} reflects the size of the magnetically interacting particles, suggesting somewhat larger particles for TFL material in $+S^0$ P. furiosus cells.

Exponentially growing P. furiosus -S⁰ cells contained only 2 - 5% high-spin Fe^{II}(O/N)₅₋₆ sites. In contrast, E. coli and B. subtilis (Gram negative and positive bacteria) contain substantially higher concentrations of such species (24). The percentage of Fe^{II}(O/N)₅₋₆ in P. furiosus -S⁰ cells increased as they shifted from exponential to stationary state. We hypothesize that imported Fe^{II} is used to assemble and install ISCs into proteins and to metallate proteins with mononuclear Fe and Fe-O-Fe active sites. Perhaps the rates of these assembly and metallation activities decline in stationary state, causing the Fe^{II} feedstock to accumulate. Under +S⁰ conditions, the demand for imported Fe^{II} may be greater (for use in generating large amounts of TFL iron), causing the level of Fe^{II} in such cells to remain low under stationary state conditions.

P. furiosus $-S^0$ cells also contain a small percentage contribution of $Fe^{II}(S)_4$ sites, corresponding to roughly 10-40 μM cellular iron. A similar concentration might be present in $+S^0$ cells but such sites could not be detected (likely due to the higher concentration of cellular iron). Table S2 indicated just two proteins that contain such sites, namely rubredoxin and rubrerythrin. This suggests an average cellular concentration of roughly 10 μM each for these proteins.

The TFL material was thought to store iron, coordinated by IssA protein in large assemblies reminiscent of how Fe^{III} is stored in ferritins (23), but other possibilities should now be considered. It seems unlikely that +S⁰ cells would store huge amounts of iron, while -S⁰ cells would store none, even when both are

grown under the same iron-replete conditions. Our experiments have shown that cells in which iron is stored as IssA-bound thioferrate cannot use it as an iron source when transferred to iron-depleted medium. In contrast, *E. coli* cells accumulate large amounts of iron as Fe^{II} (perhaps for storage), yeast accumulates Fe^{III} polyphosphate in vacuoles (34), and human cells store Fe^{III} as nanoparticles in ferritin cores (26). As a strict anaerobe, *P. furiosus* may not need to store much iron since Fe^{II} dominates the environment under anaerobic conditions and is far more soluble (and thus more bioavailable) than Fe^{III} under the more common aerobic conditions.

Clarkson et al. suggested that IssA is used to sequester insoluble iron sulfides that may be toxic to the cell, as IssA expression is sulfide specific and dependent on the presence of iron (22). The growth experiments conducted in this study support this hypothesis, as high Fe concentrations had no effect on growth of either the parent or Δ IssA in the absence of sulfide, and while iron was still predominantly stored as TFL material in the absence of IssA, the Δ IssA strain showed a significant negative growth phenotype compared to the parent under high sulfide and high Fe conditions.

[[Insert Fig. 11]]

In light of this, we tentatively propose a new role of TFL iron in the metabolism of *P. furiosus* (Figure 11). Cells grown under –S⁰ conditions use membrane-bound hydrogenase as a redox-dependent proton pump to generate a Na⁺ ion gradient that is subsequently used to generate ATP via chemiosmosis. Here, H⁺ ions are used as the terminal electron acceptor in the electron transport chain, using reducing equivalents that originated from the oxidation of either peptides or carbohydrates and then channeled through ferredoxin. Imported Fe^{II} is used to generate [Fe₄S₄] clusters, among other processes, and these are installed into various apo-proteins including hydrogenases.

Under $+S^0$ conditions, the expression level of **MBH** membrane-bound decreases. expression level of membrane-bound MBS increases (Table S3), and the rate of Fe^{II} import increases. Using reducing equivalents also obtained from peptides or carbohydrates (and also trafficked through the ferredoxin), sulfane sulfur reductase catalyzes the reduction of imported polysulfides. Thus, polysulfides serve as the terminal electron acceptor in this form of anaerobic respiration, replacing protons under +S⁰ conditions. We speculate that free short polysulfide chains are toxic to the cell, and that they react with Fe^{II} to generate the TFL material which, when bound to IssA, is less toxic to the cell. In essence, TFL iron might be a waste product of S⁰-dependent anaerobic respiration. As the cell grows, its volume increases with along an increasing concentration of the TFL iron such that the net balance of the opposing processes results in 5 – 9 mM cellular iron concentration. The rate of [Fe₄S₄] synthesis may decline under +S⁰ conditions because demand is reduced. It is intriguing to consider that this may have been an ancient respiratory pathway that dominated the early Earth in locations where elemental sulfur and ferrous ions were abundant but O2 pressures were low.

Experimental Procedures

Cell growth: Strains used in this study are listed in Table S6. Cultures for MB experiments were grown in defined maltose media composed of 1× base salts, 1× trace minerals, 1× vitamin solution, 2× 19-aminoacid solution, 0.5% (wt/vol) maltose, 0.1% (wt/vol) yeast extract, 10 μM sodium tungstate, and 0.25 mg/ml resazurin, with added cysteine at 0.5 g/l, sodium bicarbonate at 1 g/l, and 1 mM sodium phosphate buffer (pH 6.8). The 5× base salts stock solution contained (per liter) 140 g of NaCl, 17.5 g of MgSO₄·7H₂O, 13.5 g of MgCl₂·6H₂O, 1.65 g of KCl, 1.25 g of NH₄Cl, and 0.70 g of CaCl₂·2H₂O. The 1000× trace mineral stock solution contained (per

liter) 1 ml of HCl (concentrated), 0.5 g of Na₄EDTA, 0.05 g of H₃BO₃, 0.05 g of ZnCl₂, 0.03 g of CuCl₂·2H₂O, 0.05 g of MnCl₂·4H₂O 0.05 g of $(NH_4)_2M_0O_4$, 0.05AlK(SO₄)·2H₂O, 0.05 g of CoCl₂·6H₂O, and 0.05 g of NiCl₂·6H₂O. The 200× vitamin stock solution contained (per liter) 10 mg each of niacin, pantothenate, lipoic acid, aminobenzoic acid, thiamine (B₁), riboflavin (B₂), pyridoxine (B₆), and cobalamin (B₁₂) and 4 mg each of biotin and folic acid. The 25×19 amino-acid solution contained (per liter) 3.125 g each of arginine and proline; 1.25 g each of aspartic acid, glutamine, and valine; 5.0 g each of glutamic acid and glycine; 2.5 g each of asparagine, histidine, isoleucine, leucine, lysine, and threonine; 1.875 g each of alanine, methionine. phenylalanine, serine, tryptophan; and 0.3 g tyrosine. ⁵⁷Fe was added from a 50 µM stock solution prepared by dissolving 6 mg of elemental ⁵⁷Fe in 200 µl of a 1:3 HNO₃:HCl mixture. The +S⁰ conditions contained added S⁰ at 3 g/liter.

500 mL cultures were grown anaerobically in 1 liter culture bottles at 90 °C with shaking. Cells were harvested at the desired timepoints by centrifugation at 18,000×g for 10 minutes in a Beckman-Coutler Avanti J-30i centrifuge. The cell pellets were washed 3× with 2× base salts containing 50 μM sodium dithionite. Cells were loaded into MB cups and frozen at -80 °C.

For additional growth experiments, the medium was prepared as described above but with the following substitutions: yeast extract and Fe⁵⁷ were omitted from the medium, FeCl₃ was added from a 10 mM stock solution, and 50 mM 3-(N-morpholino)propanesulfonic acid (MOPS) was added. For FeS toxicity experiments, sulfide (as Na₂S) or S⁰ were added as indicated. Strains were grown in 50 mL culture bottles at 90 °C with shaking. For iron bioavailability experiments, cultures were first grown in medium containing 10 μ M iron with (WT and Δ IssA) and without (WT only) 3 g/L added S⁰. Cultures were harvested by centrifugation at 18,000×g for 10 min in a

Beckman Coulter Microfuge 22 Centrifuge. Cell pellets were washed 3× in 20 mM imidazole pH 6.5 containing 30 mM MgCl₂·6H₂O, 0.5 M KCl, 2 mM cysteine-HCl, 2 mM dithionite, and 2 mM dithiothreitol and resuspended in the same buffer. Cell suspensions were used to inoculate defined medium containing an additional 30 μM bathophenanthroline disulfonic acid. For both growth experiments, 1 ml culture samples were taken at desired time intervals, and cell protein was measured using a standard Bradford protein assay.

Mössbauer and EPR Spectroscopies: Lowfield MB spectra were collected using a model MS4 spectrometer (SEE Co., Edina MN). High-field spectra were collected at 4.2 K using a model L: He-6T spectrometer. Spectra were analyzed using WMOSS software. In spectra that contains both TFL iron and ISC doublets, the doublets were simulated using a spin Hamiltonian model (SpinHam option in WMOSS) using parameters obtained from spectra that did not contain TFL iron. Then, the area of the doublets was allowed to vary in the WinNormos program keeping all other parameters (including hyperfine) constant. Isomer shifts are reported relative to α -Fe foil at room temperature. Following MB analysis, samples were thawed in an anaerobic glovebox, transferred into EPR tubes, and refrozen. Continuous-wave X-band EPR spectra were collected using a Bruker Elexsys E500A spectrometer with a cryogen-free cooling system.

Metal and Protein Analyses: After spectra were collected, samples were thawed and transferred quantitatively to pre-weighed 15 ml Falcon tubes. Samples were resuspended in 5 mg deionized H₂O per gram of cells. Two mg of 0.5 mm diameter glass beads (Sigma) were added per mg of resuspended cell pellet, and the mixture was vortexed 3× for 30 s followed by 1 min on ice. The resulting lysate was centrifuged at 14000×g and the protein

concentration of the supernatant was determined using the Pierce BCA Protein Assay Kit (Thermoscientific). To the same supernatant was added an equal volume of trace-metal grade nitric acid, and the solution was sealed and heated overnight at 80 °C. Samples were diluted with distilled deionized water and analyzed by ICP-MS (Agilent 7700x).

Data Availability Statement: All data are contained within the manuscript and SI.

Acknowledgments: This work was supported by the National Institutes of Health (GM127021 to PAL), the National Science Foundation (MCB-1817389), the Robert A. Welch Foundation (A1170), and the Division of Chemical Sciences, Geosciences and Biosciences, Office of Basic Energy Sciences of the Department of Energy (DE-FG02-95ER20175 to MWWA). The content is solely the responsibility of the authors and does not necessarily represent the official views of the National Institutes of Health, the National Science Foundation, the Welch Foundation or the Department of Energy. We thank Dr. Francis Jenney for the gift of ⁵⁷Fe.

Conflict of interest: The authors declare that they have no conflicts of interest with the contents of this article.

FOOTNOTES

To whom corresponding should be addressed: Paul A. Lindahl, Department of Chemistry, Texas A&M University, College Station TX 77843-3255. Phone, 979-845-0956; Fax, 979-845-4719, email: Lindahl@chem.tamu.edu.

¹Texas A&M University, Department of Biochemistry and Biophysics, College Station, TX 77843 USA.

²Department of Biochemistry and Molecular Biology, University of Georgia, Athens GA 30602 USA.

³Faculty of Physics, University of Duisburg-Essen, 47057 Duisburg, Germany and Institute of Nanotechnology, Karlsruhe Institute of Technology, 76344 Eggenstein-Leopoldshafen, Germany.

⁴Texas A&M University, Department of Chemistry, College Station, TX 77843 USA.

 5 The abbreviations used are: EPR, electron paramagnetic resonance; ISC, iron sulfur cluster; MB, Mössbauer; $+S^0$, growth that includes elemental sulfur; $-S^0$, growth the excludes elemental sulfur; T_{BK} , Blocking temperature; TFL, thioferrate-like; WT, wild type.

REFERENCES

- 1. Fiala, G., and Stetter, K.O. (1986) *Pyrococcus furiosus* sp. nov represents a novel genus of marine heterotrophic archaebacteria growing optimally at 100°C. *Arch. Microbiol.* **145**, 56–61.
- 2. Cvetkovic, A., Menon, A.L., Thorgersen, M.P., Scott, J.W., Poole, F.L., Jenney, F.E., Lancaster, W.A., Praissman, J.L., Shanmukh, S., Vaccaro, B.J., Trauger, S.A., Kalisiak, E., Apon, J.V., Siuzdak, G., Yannone, S.M., Tainer, J.A., Adams, M.W.W. (2010) Microbial metalloproteomes are largely uncharacterized. *Nature* 466, 779-U18 DOI: 10.1038/nature09265
- 3. Lancaster, W.A., Praissman, J.L., Poole, F.L., Cvetkovic, A., Menon, A.L., Scott, J.W., Jenney, F.E., Jr., Thorgersen, M.P., Kalisiak, E., Apon, J.V., Trauger, S.A., Siuzdak, G., Tainer, J.A., Adams, M.W.W. (2011) A computational framework for proteome-wide pursuit and prediction of metalloproteins using ICP-MS and MS/MS data. *BMC Bioinformatics*, 12, 64 DOI: 10.1186/1471-2105-12-64.
- 4. Andreini, C., Banci, L., Bertini, I., Elmi, S. Rosato, A. (2007) Non-heme iron through the three domains of life. *Proteins-Structure and Bioinformatics* **67**, 317-324.

- 5. Robb, F.T., Maeder, D.L., Brown, J.R., DiRuggiero, J., Stump, M.D., Yeh, R.K., Weiss, R.B., and Dunn, D.M. 2001. Genomic sequence of hyperthermophile, Pyrococcus furiosus: Implications for physiology and enzymology. Methods Enzymol. 330: 134–157.
- 6. Mukund, S. and Adams, M.W.W. (1991) The novel tungsten-iron-sulfur protein of the hyperthermophilic archaebacterium, *Pyrococcus furiosus*, is an aldehyde ferredoxin oxidoreductase. Evidence for its participation in a unique glycolytic pathway. *J. Biol. Chem.* **266**, 14208-14216
- 7. Mukund S., and Adams M.W.W. (1990) Characterization of a tungsten-iron-sulfur protein exhibiting novel spectroscopic and redox properties from the hyperthermophilic archaebacterium *Pyrococcus furiosus*. *J. Biol. Chem.* **265**, 11508-11516.
- 8. Ozawa, Y., Nakamura, T., Kamata, N., Yasujima, D., Urushiyama, A., Yamakura, F., Ohmori, D., and Imai, T. (2005) *Thermococcus profundus* 2-ketoisovalerate ferredoxin oxidoreductase, a key enzyme in the archaeal energy-producing amino acid metabolic pathway. *J. Biochemistry* **137**, 101-107.
- 9. Heider, J., Mai, X., and Adams, M.W.W. (1996) Characterization of 2-ketoisovalerate ferredoxin oxidoreductase, a new and reversible coenzyme A-dependent enzyme involved in peptide fermentation by hyperthermophilic archaea. *J. Bacteriol.* **178**, 780-787.
- 10. Ma, K., Hutchins, A., Sung, S.J.S., and Adams, M.W.W. (1997) Pyruvate ferredoxin oxidoreductase from the hyperthermophilic archaeon, *Pyrococcus furiosus*, functions as a CoA-dependent pyruvate decarboxylase. *Proc. Natl. Acad. Sci. USA* **94**, 9608-9613.

- 11. Yu, H.J., Wu C.-H., Schut, G.J., Haja, D.K., Zhao, G.P., Peters J.W., Adams M.W.W., and Li, H.L. (2018) Structure of an ancient respiratory system. *Cell*, **173**, 1636–1649.
- 12. Adams, M.W.W., Holden, J.F., Menon, A.L., Schut, G.J., Grunden, A.M., Hou, C., Hutchins, A.M., Jenney, F.E., Kim, C., Ma, K.S., Pan, G.L., Roy, R., Sapra, R., Story, S.V., Verhagen, M.F.J.M. (2001) Key role for sulfur in peptide metabolism and in regulation of three hydrogenases in the hyperthermophilic archaeon *Pyrococcus furiosus*. *J. Bacteriol*. **183**, 716-724.
- 13. Schut, G.J., Bridger, S.L., and Adams, M.W.W. (2007) Insights into the metabolism of elemental sulfur by the hyperthermophilic archaeon *Pyrococcus furiosus*: characterization of a coenzyme A-dependent NAD(P)H sulfur oxidoreductase. *J. Bacteriol.* **189**, 4431–4441.
- 14. Schut, G.J., Brehm, S.D., Datta, S., and Adams, M.W.W. (2003) Whole-genome DNA microarray analysis of a hyperthermophile and an archaeon: *Pyrococcus furiosus* grown on carbohydrates or peptides. *J. Bacteriol.* **185**, 3935-3947.
- 15. Wu, C.-H., Schut, G.J., Poole, F.L., Haja, D.K., Adams, M.W.W. (2018) Characterization of membrane-bound sulfane reductase: A missing link in the evolution of modern day respiratory complexes. *J. Biol. Chem.* **293**, 16687-16696.
- 16. Lipscomb, G.L., Keese, A.M., Cowart, D.M., Schut, G.J., Thomm, M., Adams, M.W.W., Scott, R.A. (2009) SurR: a transcriptional activator and repressor controlling hydrogen and elemental sulphur metabolism in *Pyrococcus furiosus*. *Mol. Microbiol.* **71**, 332-349.

- 17. Lipscomb, G.L., Schut, G.J., Scott, R.A., Adams, M.W.W. (2017) SurR is a master regulator of the primary electron flow pathways in the order Thermococcales. *Mol. Microbiol.* **104**, 869-881.
- 18. Jenney, F.E., Adams, M.W.W. (2001) Rubredoxin from *Pyrococcus furiosus* in Hyperthermophilic Enzymes Pt. C *Methods in Enzymology* **334**, 45-55.
- 19. Weinberg, M.V., Jenney, F.E., Jr., Cui, X., and Adams, M.W.W. (2004) Rubrerythrin from the hyperthermophilic archaeon *Pyrococcus furiosus* is a rubredoxindependent, iron-containing peroxidase. *J. Bacteriol.* **186**, 7888-7895.
- 20. Strand, K.R., Sun, C.J., Jenney, F.E., Schut, G,J., and Adams M.W.W. (2010) Oxidative stress protection and the repair response to hydrogen peroxide in the hyperthermophilic archaeon *Pyrococcus furiosus* and in related species. *Arch. Microbiol.* **192**, 447-459.
- 21. Ramsay, B., Wiedenheft, B., Allen, M., Gauss, G.H., Lawrence, C.M., Young, M., and Douglas, T. (2006) Dps-like protein from the hyperthermophilic archaeon *Pyrococcus furiosus*. *J. Inorg. Biochem.* **100**, 1061–1068.
- 22. Clarkson, S.M., Newcomer, E.C., Young, E.G., and Adams, M.W.W. (2010) The elemental sulfur-responsive protein (SipA) from the hyperthermophilic archaeon *Pyrococcus furiosus* is regulated by sulfide in an iron-dependent manner. *J. Bacteriol.* **192**, 5841–5843.
- 23. Vaccaro, B.J., Clarkson, S.M., Holden, J.F., Lee, D.W., Wu, C.H., Poole, F.L., Cotelesage, J.J.H., Hackett, M.J., Mohebbi, S., Sun, J.C., Li, H.L., Johnson, M.K., George,

- G.N., and Adams, M.W.W. (2017) Biological iron-sulfur storage in a thioferrate-protein nanoparticle. *Nature Comm.* **8**, 16110; DOI: 10.1038/ncomms16110
- 24. Wofford, J.D., Bolaji, N., Dziuba, N., Outten, F.A. and Lindahl P.A. (2018) Evidence that a respiratory shield in *Escherichia coli* protects a low-molecular-mass Fe^{II} pool from O₂-dependent oxidation. *J. Biol. Chem.* **294**, 50-62.
- 25. Holmes-Hampton, G.P., Jhurry, N.D., McCormick, S.P., and Lindahl, P.A. (2013) Iron content of *Saccharomyces cerevisiae* cells grown under iron-deficient and iron-overload conditions. *Biochemistry* **52**, 105-114.
- 26. Jhurry, N.D., Chakrabarti, M., McCormick, S.P., Holmes-Hampton, G.P., and Lindahl P.A. (2012) Biophysical investigation of the ironome of human Jurkat cells and mitochondria. *Biochemistry* **51**, 5276-5284.
- 27. Gütlich, P., Bill, E., and Trautwein, A.X. (2011) Mössbauer Spectroscopy and Transition Metal Chemistry: Fundamentals and Applications. Springer Verlag, Berlin and Heidelberg, Germany.
- 28. Taft, C.A. (1977) Mössbauer studies of NaFeS₂: magnetic hyperfine fields and covalency in MFeS₂ compounds (M = Na, K, Rb, Cs). *Le Journal de Physique* **38**, 1161-1162.
- 29. Kuncser, V., Keune, W., Vopsaroiu, M., Bissell P.R. (2002) The "in-plane" angular spin distribution in layered systems as obtained by Fe-57 Mössbauer spectroscopy. *Nucl. Instr. and Meth. B* **196**, 135
- 30. Kuncser, V., Keune, W., Vopsaroiu, M., Bissell P.R. (Erratum) (2006) The 'inplane' angular spin distribution in layered systems as obtained by Fe-57 Mössbauer

- spectroscopy (vol 196, pg 135, 2002) *Nucl. Instr. and Meth. B*, **245**, 539-542.
- 31. Ramirez, A.P. (1994) Strongly geometrically frustrated magnets. *Annual Review of Materials Science*, **124**, 453-480.
- 32. Zink J. and Kagorny K. (1988) Mössbauer spectroscopic investigations of the magnetic properties of potassium thioferrate-III. *J. Phys. Chem. Solids* **49**, 1429-1434.
- 33. Mørup, S., Topsøe, H., Lipka, J. (1976) Modified theory for Mössbauer spectra of superparamagnetic particles: Application to Fe₃O₄. *Journal de Physique Colloques*, **37** (C6), C6-287-C6-290. 10.1051/jphyscol:1976658.
- 34. Cockrell A.L., Holmes-Hampton G.P., McCormick S.P., Chakrabarti M., and Lindahl P.A. (2011) Mössbauer and EPR Study of Iron in Vacuoles from Fermenting *Saccharomyces cerevisiae*. *Biochemistry*, **50**, 10275-10283.
- 35. Aono, S., Bryant, F.O., and Adams, M.W.W. (1989) A novel and remarkably thermostable ferredoxin from the hyperthermophilic archaebacterium *Pyrococcus furiosus. J. Bacteriol.* **171**, 3433-3439.
- 36. Heltzel A., Smith E.T., Zhou Z.H., Blamey J.M., Adams M.W.W. (1994) Cloning, expression, and molecular characterization of the gene encoding an extremely thermostable [4Fe-4S] ferredoxin from the hyperthermophilic archaeon *Pyrococcus furiosus*. *J. Bacteriol.* **176**, 4790–4793.
- 37. Tatur, J., Hagen, W.R., and Matias, P.M. (2006) A highly thermostable ferritin from the hyperthermophilic archaeal anaerobe *Pyrococcus furiosus*. *Extremophiles* **10**, 139-148.

- 38. Ebrahimi, K.H., Hagedoorn, P.L., Hagen, W.R. (2010) Inhibition and stimulation of formation of the ferroxidase center and the iron core in *Pyrococcus furiosus* ferritin. *J. Biol. Inorg. Chem.* **15**, 1243-1253.
- 39. Roy, R., Mukund, S., Schut G.J., Dunn D.M., Weiss, R., and Adams M.W.W. (1999) Purification and molecular characterization of tungsten-containing formaldehyde oxidoreductase ferredoxin from the hyperthermophilic archaeon **Pyrococcus** furiosus: the third of a putative five-member tungstoenzyme family. J. Bacteriol. 181, 1171-1180.
- 40. Hu Y.L., Faham S., Roy R., Adams M.W.W., and Rees D.C. (1999) Formaldehyde ferredoxin oxidoreductase from *Pyrococcus furiosus*: The 1.85 Å resolution crystal structure and its mechanistic Implications. *J. Mol. Biol.* **286**, 899-914.
- 41. Roy, R., and Adams, M.W.W. (2002) Characterization of a fourth tungstencontaining enzyme from the hyperthermophilic archaeon *Pyrococcus furiosus*. *J. Bacteriol*. **184**, 6952-6956.
- 42. Mukund S., and Adams M.W.W. (1995) Glyceraldehyde-3-phosphate ferredoxin oxidoreductase, a novel tungstencontaining enzyme with a potential glycolytic role in the hyperthermophilic archaeon *Pyrococcus furiosus*. *J. Biol. Chem.* **270**, 8389-8392.
- 43. Mai, X., and Adams, M.W.W. (1994) Indolepyruvate ferredoxin oxidoreductase from the hyperthermophilic archaeon *Pyrococcus furiosus*. A new enzyme involved in peptide fermentation. *J. Biol. Chem.* **269**, 16726-16732.

- 44. Mai X. and Adams M.W.W. (1996) Characterization of a fourth type of 2-keto acidoxidizing enzyme from a hyperthermophilic archaeon: 2-ketogluatarate ferredoxin oxidoreductase from *Thermoccoccus litoralis*. *J. Bacteriol.* **178**, 5890-5896.
- 45. Heider, J., Mai, X.H., and Adams, M.W.W. (1996) Characterization of 2-ketoisovalerate ferredoxin oxidoreductase, a new and reversible coenzyme A-dependent enzyme involved in peptide fermentation by hyperthermophilic archaea. *J. Bacteriol.* **178**, 780-787.
- 46. Sapra, R., Verhagen, M.F.J.M., and Adams, M.W.W. (2000) Purification and characterization of a membrane-bound hydrogenase from the hyperthermophilic archaeon *Pyrococcus furiosus*. *J. Bacteriol*. **182**, 3423-3428.
- 47. Yu, H, Haja, D.K., Schut, G.J., Wu, C.H., Meng, X. Zhao, G., Li, H. Adams, M.W.W. (2020) Structure of the respiratory MBS complex reveals iron-sulfur cluster catalyzed sulfane sulfur reduction in ancient life. Nature Commun. 11, Article Number: 5953 DOI: 10.1038/s41467-020-19697-7
- 48. Nguyen, D.M.N., Schut, G.J., Zadvornyy, O.A., Tokmina-Lukaszewska, M., Poudel, S., Lipscomb, G.L., Adams L.A., Dinsmore, J.T., Nixon, W.J., Boyd, E.S., Bothner, B., Peters, J.W., and Adams M.W.W. (2017) Two functionally distinct NADPCdependent ferredoxin oxidoreductases maintain the primary redox balance of Pyrococcus furiosus. J. Biol. Chem. 292, 14603-14616.
- 49. Hagen, W.R., Silva, P.J., Amorim, M.A., Hagedoorn, P.A., Wassink, H., Haaker H., and Robb, F.T. (2000) Novel structure and

- redox chemistry of the prosthetic groups of the iron-sulfur flavoprotein sulfide dehydrogenase from *Pyrococcus furiosus*; evidence for a [2Fe-2S] cluster with Asp(Cys)₃ ligands. *J. Biol. Inorg. Chem.* **5**, 527-534.
- 50. Charon, M.H., Volbeda, A., Chabriere, E., Pieulle, L., and Fontecilla-Camps, J.C. (1999) Structure and electron transfer mechanism of pyruvate:ferredoxin oxidoreductase. *Curr Opin Struct Biol* **9**, 663–669.
- 51. Blamey, J.M. and Adams, M.W.W. (1993) Purification and characterization of pyruvate ferredoxin oxidoreductase from the hyperthermophilic archaeon *Pyrococcus furiosus*. *B.B.A.-Protein Struct*. *M.* **1161**, 19-27.
- 52. Kurihara, K., Tanaka, I., Chatake, T., Adams, M.W., Jenney, F.E, Jr, Moiseeva N., Bau R, Niimura N. (2004) Neutron crystallographic study on rubredoxin from *Pyrococcus furiosus* by BIX-3, a single-crystal diffractometer for biomacromolecules. *Proc. Natl. Acad. Sci. U.S.A.* **101**, 11215–11220.
- 53. Bryant, F.O., and Adams, M.W.W. (1989) Characterization of hydrogenase from the hyperthermophilic archaebacterium, *Pyrococcus furiosus*. *J. Biol. Chem.* **264**, 5070-5079.
- 54. Ma, K., Weiss, R., and Adams, M.W.W. (2000) Characterization of hydrogenase II from the hyperthermophilic archaeon *Pyrococcus furiosus* and assessment of its role in sulfur reduction. *J. Bacteriol.* **182**, 1864-1871.
- 55. Yeh, A.P., Hu, Y., Jenney, F.E., Adams, M.W.W., and Rees, D.C. (2000) Structures of the superoxide reductase from

Pyrococcus furiosus in the oxidized and reduced states. Biochemistry **39**, 2499-2508.

- 56. Clay, M.D., Jenney, F.E., Jr., Hagedoorn, P.L., George, G.N., Adams, M.W. W., and Johnson, M.K. (2002) Spectroscopic studies of *Pyrococcus furiosus* superoxide reductase: Implications for active-site structures and the catalytic mechanism. *J. Am. Chem. Soc.* **124**, 788-805.
- 57. Jenney, F.E., Jr., Verhagen, M.F.J.M., Cui, X., and Adams, M.W.W. (1999) Anaerobic microbes: oxygen detoxification without superoxide dismutase. *Science* **286**, 306-309.
- 58. Sevcenco, A.M., Bevers, L.E., Pinkse, M.W.H., Krijger, G.C., Wolterbeek, H.T., Verhaert, P.D.E.M., Hagen, W.R., and Hagedoorn, P.L. (2010) Molybdenum incorporation in tungsten aldehyde oxidoreductase enzymes from *Pyrococcus furiosus*. *J. Bacteriol.* **192**, 4143-4152.
- 59. Lipscomb, G.L., Stirrett, K., Schut, G.J., Yang, F., Jenney, F.E. Jr, Scott, R.A., Adams M.W.W, Westpheling, J. (2011) Natural competence in the hyperthermophilic archaeon *Pyrococcus furiosus* facilitates genetic manipulation: construction of markerless deletions of genes encoding the two cytoplasmic hydrogenases. *Appl Environ Microbiol.* 77, 2232-2238.
- 60. Bridger, S.L., Clarkson, S.M., Stirrett, K., DeBarry, M.B., Lipscomb, G.L., Schut G.J., Westpheling, J., Scott, R.A., Adams, M.W.W. (2011) Deletion strains reveal metabolic roles for key elemental sulfurresponsive proteins in *Pyrococcus furiosus*. *J Bacteriol*. **193**, 6498-6504.

Table 1: Mössbauer parameters used in simulations (Averaged), LT- Low Temperature and HT – High Temperature.

	ISCw	ISC _N	Magnetic (S ⁰ -dependent)	Magnetic (other)	Fe(S ₄)	Fe ^{II} (O/N)	$S = 5/2 \text{ Fe}^{III}$
δ (mm/s)	$0.45 \pm 0.04 \text{ (LT)} \\ 0.43 \pm 0.03 \text{ (HT)}$	$0.43 \pm 0.03 \text{ (LT)} \\ 0.38 \pm 0.05 \text{ (HT)}$			0.65 ± 0.04	$1.3 \pm 0.1 \text{ (LT)}$	0.50±0.02
						$1.2 \pm 0.1 (HT)$	
ΔE_Q (mm/s)	$1.35 \pm 0.05 (LT)$	$0.83 \pm 0.06 (LT)$			3.0 ± 0.05	$2.6 \pm 0.1 (LT)$	0.45±0.02
	$1.15 \pm 0.1 \text{ (HT)}$	0.75 ± 0.07 (HT)				$2.7 \pm 0.1 (HT)$	
Γ (mm/s)	$0.34 \pm 0.06 (LT)$	$0.47 \pm 0.04 (LT)$			0.43 ± 0.03	$0.5 \pm 0.1 \text{ (LT)}$	0.50±0.05
	$0.35 \pm 0.05 (HT)$	$0.45 \pm 0.04 (HT)$				$0.5 \pm 0.1 (HT)$	
D; E/D							0.5; 0.33
$A_x; A_y; A_z$							-29.08 MHz
η							2.5±0.5
$\mathbf{g}_{\mathbf{x}},\mathbf{g}_{\mathbf{y}},\mathbf{g}_{\mathbf{z}}$							2.0
Figure 1	45% (LT) 35% (HT) 43% (Post Storage)	35% (LT) 60% (HT) 33% (Post Storage)		~14-15% (LT)		4-5% (LT) 4-5% (HT) 8% (Post storage)	16% (Post storage)
Figure 3	10% (LT) 33% (HT)	10% (LT) 65% (HT)	78% (LT)			2% (LT) 2% (HT)	
Figure 6	+S ⁰ 10% (LT) 35% (LT) -S ⁰ 52% (LT) 42% (HT)	10% (LT) 63% (HT) 23% (LT) 33% (HT)	77% (LT)		2% (LT) 2% (HT)	3% (LT) 3% (LT) 23% (LT) 23% (HT)	
Figure 7	49% (5 K) 44% (150 K)	36% (5 K) 41% (150 K)			3% (LT) 3% (HT)	12% (5 K) 12% (150 K)	

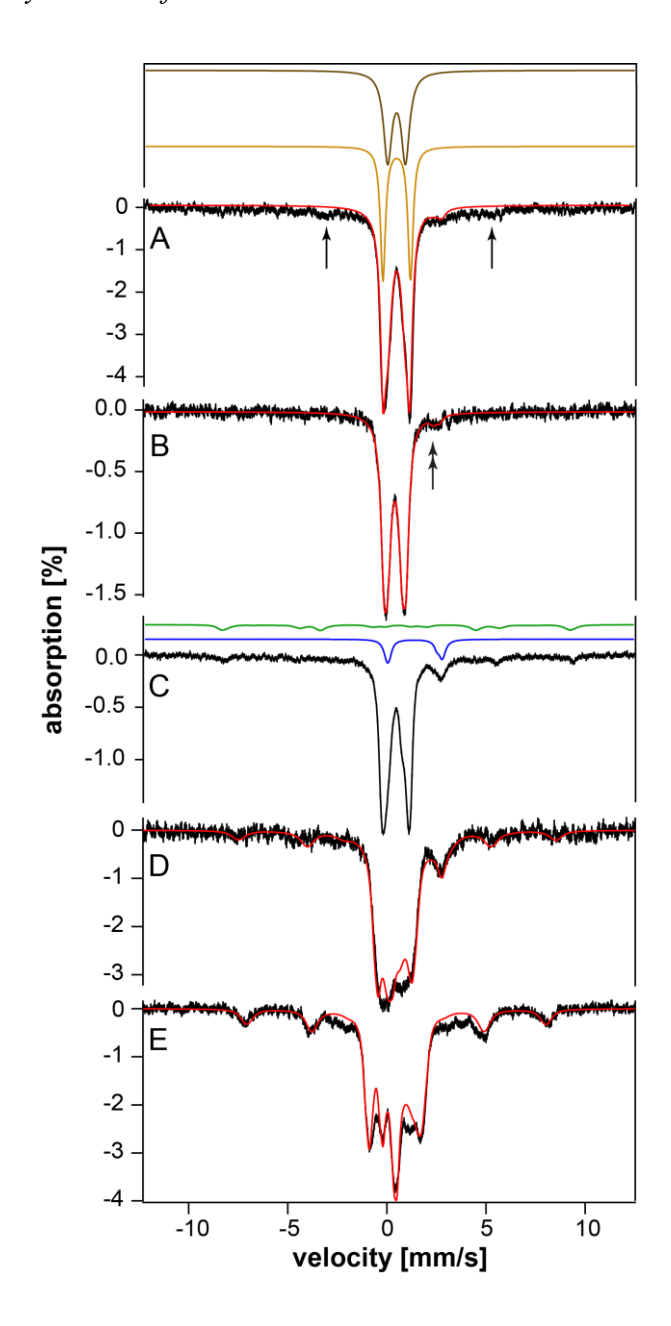


Figure 1: Mössbauer spectra of WT *P. furiosus* cells grown under -S 0 conditions and harvested during exponential growth. A, 5 K, 0.05 T; B, 150 K, 0.05 T; C, 4.2 K, 0 T; D, 4.2 K, 3.0 T; and E, 4.2 K, 6.0 T. The field was applied parallel (A and B) and perpendicular (C – E) to the gamma radiation.

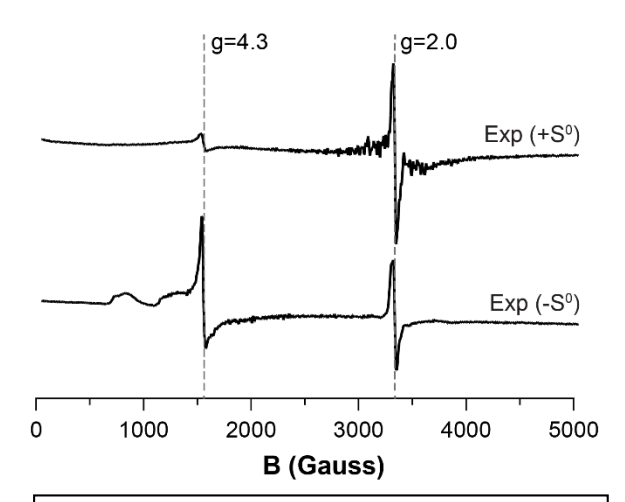


Figure 2: EPR spectra of WT cells grown under $+S^0$ (top) and $-S^0$ (bottom) conditions. EPR conditions: T, 4 K; frequency, 9.36 GHz; microwave power, 0.2 mW; modulation amplitude 10 G; modulation frequency 100 KHz; sweep time 300s

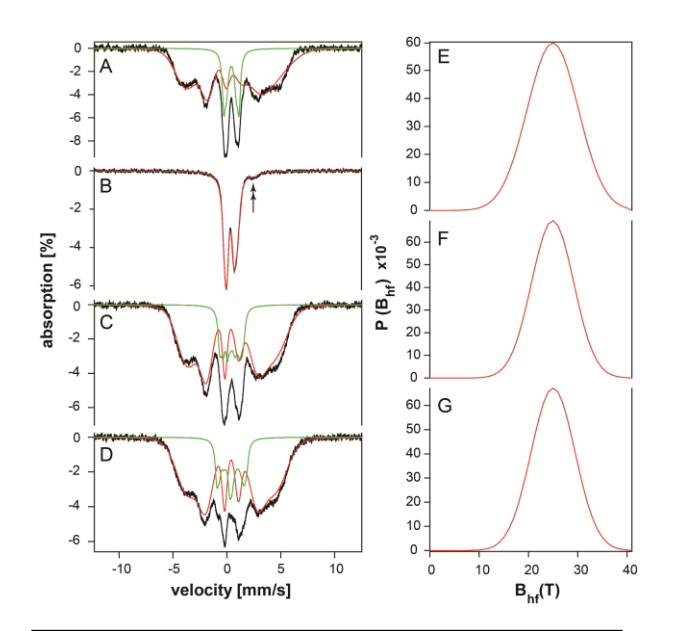


Figure 3: Mössbauer spectra of the WT+S 0 sample grown with 10 μ M 57 Fe and S 0 in the medium, and harvested during exponential phase. A, 5 K 0.05 T; B, 150 K; C, 4.2 K and 3 T; D, 4.2 K and 6.0 T. The applied magnetic field was perpendicular to the gamma radiation. The red lines in A, C, and D are simulations of the magnetically ordered iron using the continuous distribution of hyperfine fields in E (0.05 T), F (3 T) and G (6T). Green solid lines are simulations to WCD and NCD contributions assuming 20% spectral intensity.

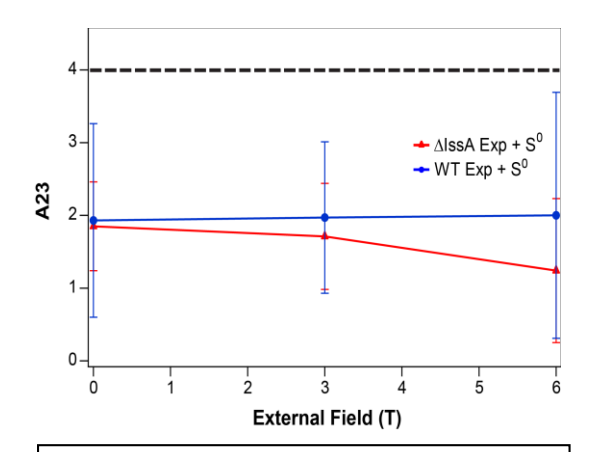


Figure 4: Plot of A_{23} vs external field for WT+S⁰ exponential cells (blue line) and $\Delta IssA+S^0$ exponential cells (red line).

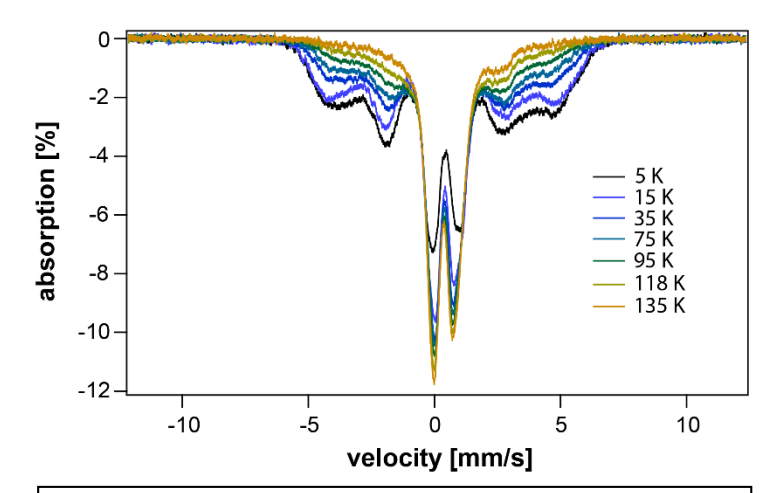


Figure 5: Low-field (0.05 T) Mössbauer spectra of exponentially harvested WT+S⁰ cells collected at increasing temperatures.

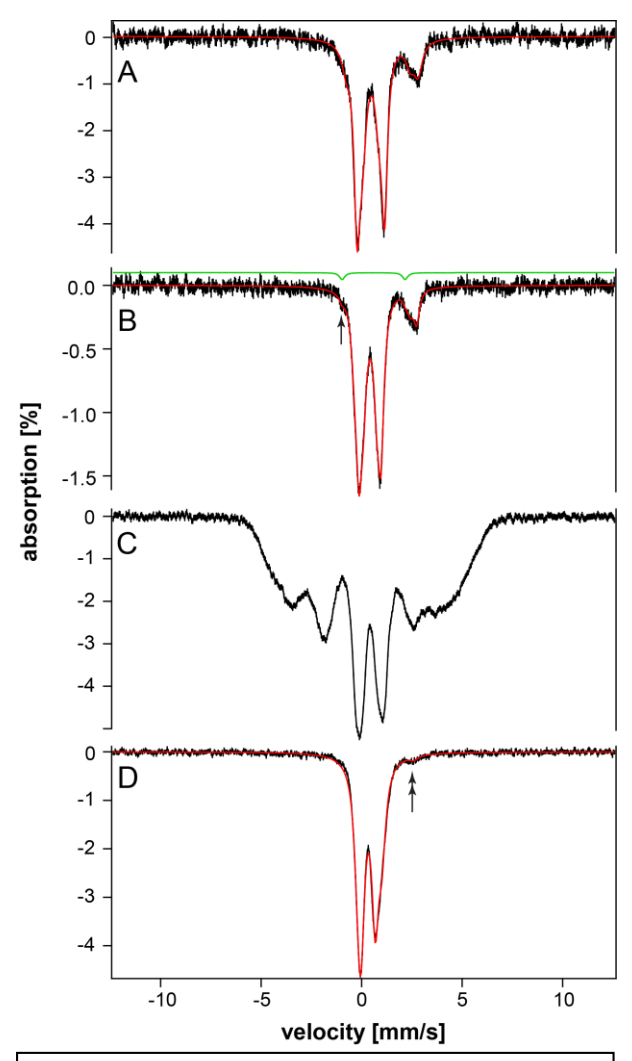


Figure 6: Low-field (0.05 T) Mössbauer spectra of WT-S⁰ (A and B) and WT+S⁰ (C and D) harvested after cells had reached stationary state. A and C, 5 K; B and D, 150 K.

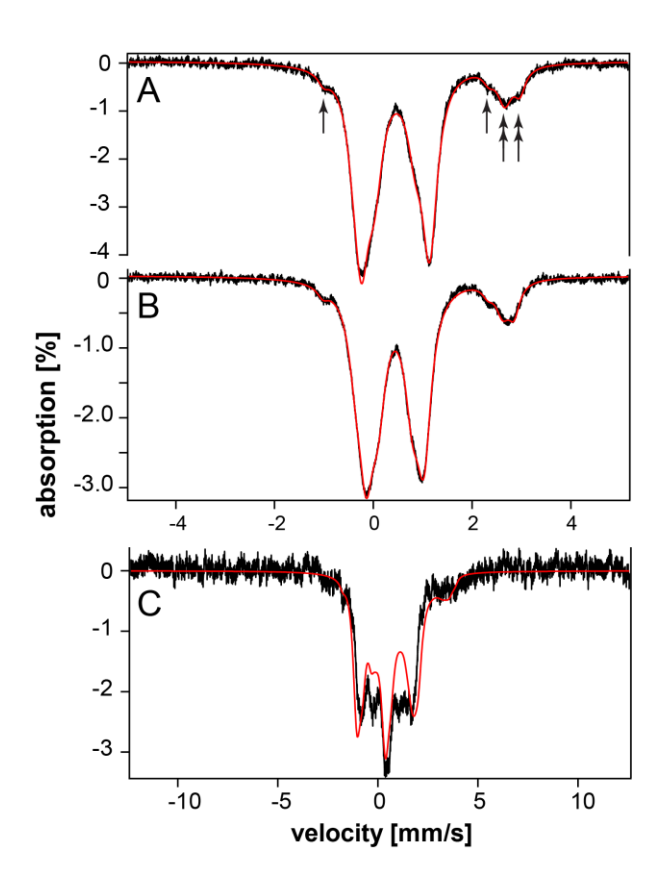


Figure 7: Mössbauer Spectra of $\Delta IssA\text{-}S^0$ cells. A, 10 K and 0.05 T; B, 150 K and 0.05 T; C, 4.2 K and 6.0 T.

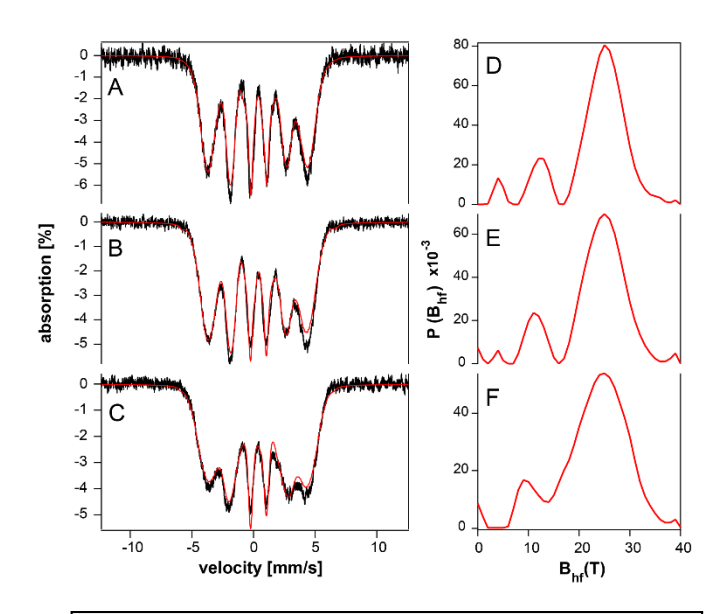


Figure 8: 4.2 K Mössbauer spectra of $\Delta IssA+S^0$ cells at A, 0; B, 3.0; and C, 6.0 T. Unconstrained histogram distributions are shown in D (0 T), E (3 T) and F (6 T).

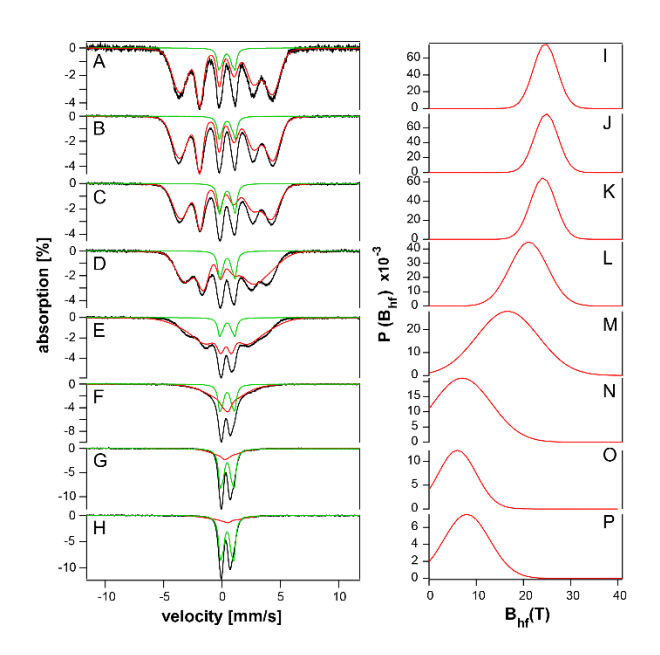


Figure 9: Variable Temperature 0.05 T Mössbauer spectra of $\Delta IssA+S^0$ cells. Right column shows the B_{hf} distribution used to obtain the fit. A and I, 5 K; B and J, 10 K; C and K, 25 K; D and L, 40 K; E and M, 55 K; F and N, 70 K; G and O, 100 K; H and P, 120K. Solid green lines in the left column show contribution from $ISC_{N/W}$ while solid red lines indicate contribution from TFL.

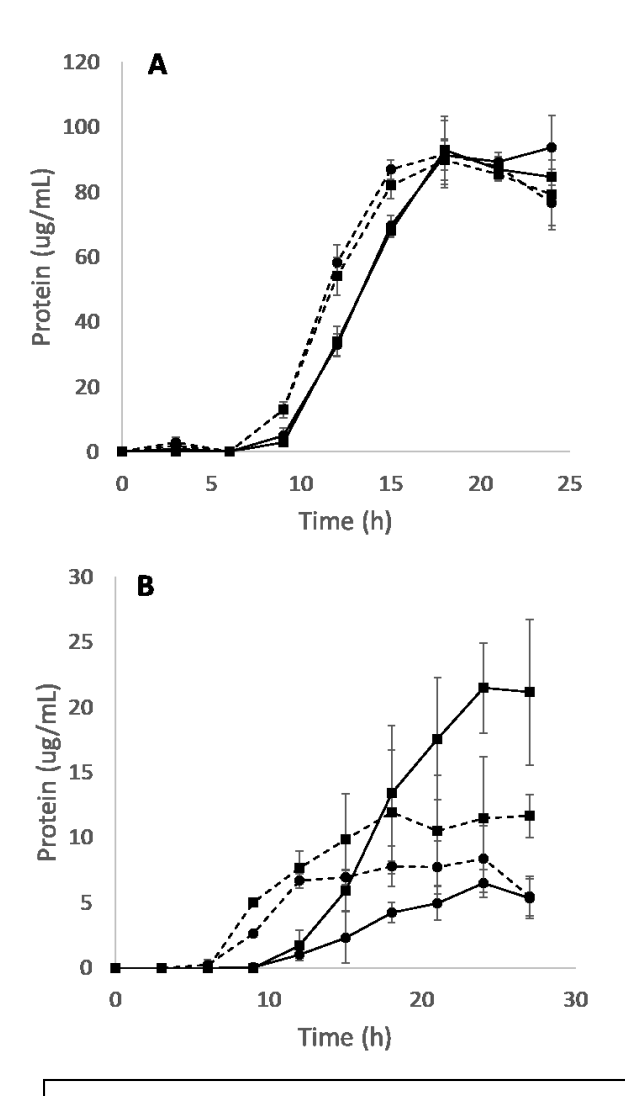


Figure 10: Growth of *Pyrococcus furiosus* with 10 mM Na₂S (top panel) and 1 g/l S⁰ (bottom panel) conditions (on maltose). Solid lines, WT; dashed lines, $\Delta IssA$; (\blacksquare), 10 μM Fe; (\bullet), 50 μM Fe. Error bars represent standard deviation of biological triplicate samples.

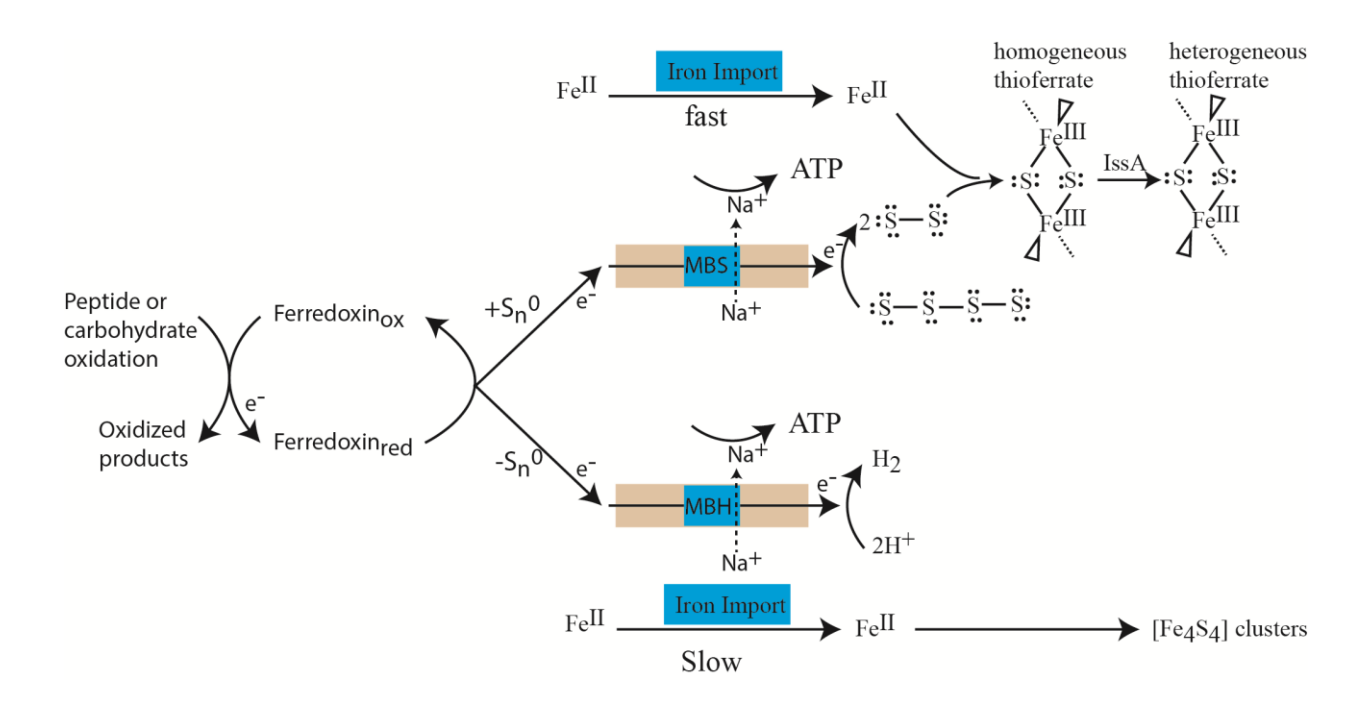


Figure 11: A Model of cellular energy metabolism emphasizing the role of iron and elemental sulfur in *P. furiosus*. See text for details.

Supporting Information

Manuscript title: The *Pyrococcus furiosus* ironome is dominated by [Fe₄S₄]²⁺ clusters or thioferrate-like iron depending on the availability of elemental sulfur

Authors: Shaik Waseem Vali, Dominik K. Haja, Richard A. Brand, Michael W. W. Adams, and Paul A. Lindahl

Table of Contents:

Table S1 Iron-containing proteins in *Pyrococcus furiosus* predicted by bioinformatics.

Table S2: Characterized iron-containing proteins in *Pyrococcus furiosus*.

Table S3: Proteins upregulated under $+S^0$ conditions.

Table S5. Cellular elemental concentrations of samples.

Table S1 Iron-containing proteins in *Pyrococcus furiosus* predicted by bioinformatics. Taken from (3).

(3).				
	GM Number	ORF Number	Annotation	
1	PF0754	748906	2-keto acid:ferredoxin oxidoreductase subunitalpha	
2	PF1768	1645457	2-keto acid:ferredoxin oxidoreductase subunitalpha	
3	PF1771	1647980	2-keto acid:ferredoxin oxidoreductase subunitalpha	
4	PF0845	817300	2-keto acid:ferredoxin oxidoreductase subunitalpha	
5	PF1767	1644264	2-keto acid:ferredoxin oxidoreductase subunitdelta	
6	PF1770	1646824	2-keto acid:ferredoxin oxidoreductase subunitgamma	
7	PF1773	1649361	2-keto acid:ferredoxin oxidoreductase subunitgamma	
8	PF0139	149451	2-keto acid:ferredoxin oxidoreductase subunitgamma	
9	PF0969	928888	2-ketovalerate ferredoxin oxidoreductase subunitalpha-2	
10	PF0970	930085	2-ketovalerate ferredoxin oxidoreductase subunitdelta-2	
11	PF0938	903832	3-isopropylmalate dehydratase large subunit	
12	PF0511	530974	3-methyladenine DNA glycosylase	
13	PF0201	214120	aconitate hydratase (aconitase)	
14	PF0075	81500	alcohol dehydrogenase	
15	PF0608	631178	alcohol dehydrogenase	
16	PF0346	358419	aldehyde:ferredoxin oxidoreductase (aor)	
17	PF1033	989258	alkyl hydroperoxide reductase	
18	PF0722	720985	alkyl hydroperoxide reductase subunit c	
19	PF2064	1904500	arylsulfatase regulatory protein, putative	
20	PF0077	83155	biotin operon repressor/biotin[acetyl CoAcarboxylase] ligase	
21	PF0860	835631	btpA family protein	
22	PF0482	497978	cell division control protein 21	
23	PF0302	318028	co-factor modifying protein	
24	PF0204	220427	conserved hypothetical protein	
25	PF0206	222756	conserved hypothetical protein	
26	PF0096	104208	conserved hypothetical protein	
27	PF1182	1128650	conserved hypothetical protein	
28	PF1489	1391238	conserved hypothetical protein	
29	PF1551	1448377	conserved hypothetical protein	
30	PF1158	1107110	conserved hypothetical protein	
31	PF1061	1016054	conserved hypothetical protein	
32	PF0037	43228	conserved hypothetical protein	
33	PF1192	1137142	conserved hypothetical protein	
34	PF1193	1137512	conserved hypothetical protein	
35	PF1199	1141457	conserved hypothetical protein	
36	PF1544	1443272	conserved hypothetical protein	
37	PF1397	1311770	conserved hypothetical protein	
38	PF1049	1002916	conserved hypothetical protein	

39	PF1083	1032190	conserved hypothetical protein
40	PF2025	1871822	conserved hypothetical protein
41	PF0144	154650	conserved hypothetical protein
42	PF1638	1529201	conserved hypothetical protein
43	PF0138	148781	conserved hypothetical protein
44	PF0850	824641	conserved hypothetical protein
45	PF1718	1597514	conserved hypothetical protein
46	PF1325	1247070	conserved hypothetical protein
47	PF1285	1211743	conserved hypothetical protein
48	PF1286	1212834	conserved hypothetical protein
49	PF1277	1207631	conserved hypothetical protein
50	PF0913	884008	conserved hypothetical protein
51	PF0914	884391	conserved hypothetical protein
52	PF0843	816518	conserved hypothetical protein
53	PF0846	820618	conserved hypothetical protein
54	PF0849	823503	conserved hypothetical protein
55	PF1389	1302837	conserved hypothetical protein
56	PF1454	1362012	conserved hypothetical protein
57	PF1470	1375936	conserved hypothetical protein
58	PF1190	1136390	conserved hypothetical protein
59	PF1195	1138566	conserved hypothetical protein
60	PF1196	1139695	conserved hypothetical protein
61	PF0689	700021	conserved hypothetical protein
62	PF0695	705210	conserved hypothetical protein
63	PF0741	738742	conserved hypothetical protein
64	PF0723	722156	conserved hypothetical protein
65	PF1934	1783451	conserved hypothetical protein
66	PF1972	1822760	conserved hypothetical protein
67	PF1628	1520292	conserved hypothetical protein
68	PF0342	354894	conserved hypothetical protein
69	PF1605	1496972	conserved hypothetical protein
70	PF0612	633007	conserved hypothetical protein
71	PF1914	1765399	conserved hypothetical protein
72	PF1042	996088	conserved hypothetical protein
73	PF1967	1817174	conserved hypothetical protein
74	PF0602	622998	conserved hypothetical protein
75	PF0631	643597	conserved hypothetical protein
76	PF1782	1655977	conserved hypothetical protein
77	PF2033	1877126	conserved hypothetical protein
78	PF0858	833697	conserved hypothetical protein
79	PF0724	722839	conserved hypothetical protein

		Т		
80	PF0690	699847	conserved hypothetical protein, possiblethioredoxin/glutaredoxin	
81	PF0731	727122	copper-transporting atpase, p-type	
82	PF0705	709009	cytochrome c-type biogenesis protein	
83	PF1242	1175771	dehydrogenase subunit alpha	
84	PF1296	1223405	dihydropteroate synthase	
85	PF1941	1793572	dihydropteroate synthase	
86	PF0942	908597	dihydroxy-acid dehydratase	
87	PF1210	1152634	dipeptide ABC transporter, permease protein	
88	PF1797	1669334	d-nopaline dehydrogenase	
89	PF1909	1760272	ferredoxin	
90	PF2030	1873914	ferredoxin-family protein	
91	PF0857	831703	ferrous iron transport protein b	
92	PF0751	746296	flavoprotein	
93	PF0694	703868	flavoprotein	
94	PF1203	1145403	formaldehyde:ferredoxin oxidoreductase	
95	PF1480	1385199	formaldehyde:ferredoxin oxidoreductase wor5	
96	PF1521	1419794	formate dehydrogenase alpha chain	
97	PF0441	457188	galactose-1-phosphate uridylyltransferase	
98	PF1910	1760551	glutamate synthase	
99	PF0205	221932	32 glutamate synthase subunit alpha	
100	PF1327	1247601		
101	PF1457	1363259	glutaredoxin/thioredoxin-like protein	
102	PF0094	102519	glutaredoxin-like protein	
103	PF0464	478142	glyceraldehyde-3-phosphate:ferredoxinoxidoreductase	
104	PF2005	1855892	glycerol-3-phosphate dehydrogenase	
105	PF1229	1162991	glycosylase putative; mutY-nth family	
106	PF1763	1640658	GTP-binding protein, gtp1/obg family	
107	PF0925	890633	heme biosynthesis protein	
108	PF0647	659796	heme biosynthesis protein	
109	PF1332	1253842	H-II alpha (hydrogenase subunit alpha)	
110	PF1331	1252601	H-II delta (hydrogenase subunit delta)	
111	PF1330	1251888	H-II gamma (hydrogenase subunit gamma)	
112	PF1329	1251025	H-II hydrogenase subunit beta	
113	PF0008	8548	hit family protein (hit)	
114	PF1107	1054030	hit family protein (hit)	
115	PF0559	577932	hydrogenase expression/formation regulatoryprotein	
116	PF0188	198787	hydrogenase subunit gamma	
117	PF1328	1249026	hydrogenase subunit gamma	
118	PF1245	1179923	hypothetical d-nopaline dehydrogenase	
119	PF1109	1058861	hypothetical protein	
120	PF1482	1386082	hypothetical protein	

121	PF2060	1899840	hypothetical protein	
122	PF1110	1059349	hypothetical protein	
123	PF0533	551149	indolepyruvate ferredoxin oxidoreductase subunita	
124	PF0534	551790	indolepyruvate ferredoxin oxidoreductase subunitb	
125	PF1774	1650532	iron (III) ABC transporter, ATP-binding protein	
126	PF0911	882732	iron (III) ABC transporter, ATP-binding protein	
127	PF0851	825121	iron-dependent repressor	
128	PF0660	671023	iron-sulfur cluster binding protein	
129	PF1952	1802989	iron-sulfur protein	
130	PF1976	1828270	1-aspartate oxidase (quinolinate synthetase)	
131	PF1432	1342256	mbh10 NADH dehydrogenase subunit (like cCoL,EchC, HycH)	
			mbh12 membrane bound hydrogenase alpha	
132	PF1434	1344050	(NADHdehydrogenase)	
133	PF1436	1345434	mbh14 iron-sulfur protein (like HycF, EchF,CooX)	
134	PF0090	97550	molybdenum cofactor biosynthesis protein	
135	PF0345	358122	molybdopterin converting factor, subunit 1	
136	PF0543	562899	molybdopterin converting factor, subunit 1	
137	PF0729	725885	multi domain protein containingcorrinoid/iron-sulfur region	
138	PF1444	1352727	NADH dehydrogenase subunit	
139	PF1441	1350388		
140	PF1442	1351020	20 NADH dehydrogenase subunit	
141	PF1901	1751973	oxygen-independent coproporphyrinogen IIIoxidase	
142	PF1003	961250	phosphate-binding periplasmic protein precursor(pbp)	
143	PF1755	1632493	possible fumarate hydratase (fumarase) alphasubunit	
144	PF1754	1632002	possible fumarate hydratase (fumarase) betasubunit	
145	PF0692	702081	prismane protein homolog	
146	PF1287	1214251	probable ATP-dependent transporter similar toabc	
147	PF0742	739367	probable ferritin homolog	
148	PF1903	1754483	probable translation initiation factor (if-2homolog)	
149	PF1679	1562997	putative 3-isopropylmalate dehydratase largesubunit	
150	PF1680	1563488	putative 3-isopropylmalate dehydratase smallsubunit	
151	PF0939	904323	putative 3-isopropylmalate dehydratase smallsubunit	
152	PF0187	197868	putative cofactor synthesis protein	
153	PF0247	256063	putative HTH transcription regulator	
154	PF1911	1761982	putative hydrogenase	
155	PF1479	1383440	putative oxidoreductase, Fe-S subunit	
156	PF0119	123510	putative perplasmic sugar binding protein	
157	PF1796	1669077	putative polyferredoxin	
158	PF2026	1872873	putative polyferredoxin	
159	PF1938	1788984	putative sugar binding protein (malE-like)	
160	PF0966	926380	pyruvate ferredoxin oxidoreductase subunitalpha-2	
161	PF0967	927581	pyruvate ferredoxin oxidoreductase subunitdelta	

162	PF0971	930439	pyruvate ferredoxinoxidoreductase/2-ketovalerate ferredoxin oxidoreductasegamma subunit	
163	PF0670	679716	rnase l inhibitor	
164	PF1282	1210573	rubredoxin	
165	PF1283	1210814	rubrerythrin	
166	PF1795	1668574	sarcosine oxidase subunit alpha	
167	PF0894	867811	sulfhydrogenase alpha subunit	
168	PF0891	864857	sulfhydrogenase beta subunit	
169	PF0893	866528	sulfhydrogenase delta subunit	
170	PF0892	865732	sulfhydrogenase gamma subunit	
171	PF1281	1210188	superoxide reductase	
172	PF0752	747589	thioredoxin peroxidase	
173	PF1337	1257851	transcriptional activator, putative	
174	PF1338	1258479	transcriptional activator, putative	
175	PF1194	1138558	transcriptional regulator (furr family)	
176	PF1739	1616027	trehalose/maltose binding protein	
177	PF0344	356987	tungsten-containing aldehyde ferredoxinoxidoreductase cofactor modifying protein	
178	PF1961	1812948	tungsten-containing formaldehyde ferredoxinoxidoreductase wor4	

Table S2: Characterized iron-containing proteins in *Pyrococcus furiosus*.

Protein	Identifier	Description	Iron Center	Reference
Aldehyde ferredoxin Oxidoreductase (AOR)	PF0346	Oxidizes aldehydes derived from amino acids	1 [Fe ₄ S ₄] per subunit; 1 Fe ^{II} per dimer	(6)
DPS-like Protein (miniferritin)	PF1193	Peroxidase activity; H ₂ O ₂ oxidation of Fe ^{II}	[Fe-O-Fe] ferroxidase site; ca. 300 Fe ^{III} ions in mineral aggregate	(20,21)
Dehydratase	PF0938 PF1679	Involved in amino acid biosynthesis	Predicted to encode an ISC	(20)
Dipeptide binding protein	PF0357		Predicted to encode an ISC	(20)
Ferredoxin (Fd)	PF1909	Redox currency	[Fe ₄ S ₄] ^{2+/1+} cluster coordinated by 3 cys and 1 asp	(35,36)
Ferritin	PF0742	Iron storage	[Fe-O-Fe] ferroxidase site; thousands of Fe ^{III} ions in ferrihydrite-like mineral	(37,38)
Formadehyde ferrodoxin oxidoreductase (FOR)	PF1203	Oxidizes aldehydes in the catabolism of amino acids	1 [Fe ₄ S ₄]	(39,40)
Formaldehyde ferredoxin oxidoreductase 4 (WOR4)	PF1961	Unknown; maybe involved in S ⁰ reduction	1 [Fe ₄ S ₄]	(41)
Formate dehydrogenase (putative	PF1242 PF1521			
Glyceraldehyde-3- Phosphate ferredoxin oxidoreductase (GAPOR)	PF0464	Involved in the unusual glycolytic pathway in Pf (metabolism of carbohydrates). This converts glyceraldehyde-3-phosphate to glycerate-	1 [Fe ₄ S ₄]	(42)

		3-phosphate without generating ATP. Ferredoxin is the electron acceptor in glycolysis; no NAD(P)H is formed.		
Indolepyruvate ferredoxin oxidoreductase (IOR)	PF0533 PF0534	Catalyzes the oxidative decarboxylation of aryl pyruvates generated by the transamination of aromatic amino acids, to the corresponding aryl acetyl-CoA (same as PFOR).	Each tetramer contains 4 [Fe ₄ S ₄] clusters and 1 [Fe ₃ S ₄] cluster	(43)
Iron-sulfur storage protein A (IssA)	PF2025	Upregulated when grown on S ⁰ and iron	Associated with thioferrate aggregates	(22,23)
3-isopropylmalate dehydratase	PF0938 PF0939			(14)
2-ketoglurate ferredoxin oxidoreductase (KGOR)	PF1767 PF1768 PF1769 PF1770	Catalyzes the oxidative decarboxylation of 2-ketoglutarate to succinyl coenzyme A and CO ₂ and reduces ferredoxin; involved in biosynthesis not energy (homolog of PFOR).	3 [Fe ₄ S ₄] clusters	(44)
2-ketoisovalerate ferredoxin oxidoreductase (VOR)	PF0968 PF0969 PF0970 PF0971	Catalyzes the oxidative decarbonylation of mainly aliphatic aminoacid derived 2-keto acids.	3 [Fe ₄ S ₄] clusters	(45)

Protein	Identifier	Description	Iron Center	Reference
Membrane-bound hydrogenase (MBH)	PF1423 PF1424 PF1425 PF1426 PF1427 PF1428 PF1429 PF1430 PF1431 PF1431 PF1432 PF1433 PF1434 PF1435 PF1436	Used in energy generation. Related to Respiratory Complex I	3 [Fe ₄ S ₄] + NiFe site	(46) (11)
Membrane-bound sulfane reductase (MBS)	PF1441 PF1442 PF1443 PF1444 PF1445 PF1446 PF1447 PF1448 PF1449 PF1450 PF1451 PF1452 PF1453	Homolog of MBH complex. Expression increases after S ⁰ addition. MBX reduces the sulfane sulfur of polysulfides.	3 [Fe ₄ S ₄] clusters	(47)
NADH-dependent reduced ferredoxin:NADP ⁺ oxidoreductase 1 (Nfn1)	PF1327 PF1328	Electron bifurcation	1 [Fe ₂ S ₂] + 2 [Fe ₄ S ₄]	(48,49)
NADH-dependent reduced ferredoxin:NADP ⁺ oxidoreductase 2 (NfnII)	PF1910 PF1911	Shuttles electrons between NADPH and Fd. Uprelated under S0 reducing conditions with sugars or peptides as carbon sources.	1 [Fe ₂ S ₂] + 2 [Fe ₄ S ₄]	(48,49)
Prismane protein	PF0692		Predicted to encode an ISC	(20)
Pyruvate ferredoxin oxidoreductase (POR or PFOR)	PF0965 PF0966 PF0967 PF0971	Catalyzes the ferredoxin-dependent oxidative decarboxylation of pyruvate to acetyl-CoA.	3 [Fe ₄ S ₄] clusters	(50,51)
Rubredoxin	PF1282	Donates electrons to rubrerythrin and superoxide reductase. Is involved in an anaerobic ROS detoxification system.	Fe(cys)4	(52)
Rubrerythrin	PF1283	Catalyzes the reduction of H ₂ O ₂ to water using electrons from rubredoxin; involved in anaerobic ROS detoxification.	1 [Fe-O-Fe] and 1 Fe(cys)4	(19)
Soluble Hydrogenase I (SHI)	PF0891 PF0892 PF0893 PF0894	Catalyzes the reversible oxidation of H ₂ to generate reduced NAD(P)H	3 [Fe ₄ S ₄] + NiFe site	(53)
Soluble Hydrogenase II (SHII)	PF1329 PF1330 PF1331 PF1332	Catalyzes the reversible oxidation of H ₂ to generate reduced NAD(P)H	3 [Fe ₄ S ₄] + NiFe site	(54)
Superoxide reductase	PF1281	Catalyzes the reduction of superoxide to H ₂ O ₂ using rubredoxin as an electron donor.	Mononuclear Fe ^{II} with 4 His, 1 Ccys, and 1 Glu ligand.	(55,56,57)

WOR5	PF1480	4 [Fe ₄ S ₄]	(58)

Table S3: Proteins upregulated under $+S^0$ conditions (fold change >3). Taken from (14).

Gene	Annotation	Avg_Log2_Ratio	SD	Fold
PF2025	IssA	7.568	0.456	189.852
PF2026	putative polyferredoxin	6.573	1.728	95.265
PF0938	3-isopropylmalate dehydratase large subunit	3.406	0.403	10.603
PF0094	glutaredoxin-like protein	3.333	0.564	10.081
PF1972	ribonucleoside-triphosphate reductase activating protein	3.035	0.185	8.199
PF0723	FTR1 Iron Permease	2.947	0.051	7.711
PF0942	dihydroxy-acid dehydratase	2.699	0.093	6.496
PF0939	putative 3-isopropylmalate dehydratase smallsubunit	2.294	0.186	4.907
PF2030	ferredoxin-family protein	2.098	0.155	4.281
PF0857	ferrous iron transport protein b	2.056	0.022	4.16
PF0075	alcohol dehydrogenase	1.927	0.286	3.803
PF0204	glutamine amidotransferase type-2 domain- containing protein	1.641	0.032	3.12
PF1454	radical SAM containing protein	1.623	0.059	3.082

Table S4: Proteins upregulated during $-S^0$ conditions (fold change > 3). Taken from (14).

Gene	Annotation	Avg_Log2_Ratio	SD	Fold
PF0925	heme biosynthesis protein	-6.012	0.21	64.565
PF1329	H-II hydrogenase subunit beta	-5.935	1.146	61.2
PF1330	H-II gamma (hydrogenase subunit gamma)	-5.891	0.584	59.367
PF2064	arylsulfatase regulatory protein, putative	-5.632	0.288	49.597
PF1521	formate dehydrogenase alpha chain	-5.545	0.1	46.707
PF1331	H-II delta (hydrogenase subunit delta)	-5.208	0.237	36.968
PF0891	sulfhydrogenase beta subunit	-4.391	0.783	20.982
PF1797	d-nopaline dehydrogenase	-4.138	0.993	17.611
PF1332	H-II alpha (hydrogenase subunit alpha)	-3.868	2.406	14.603
PF1482	MoaD/ThiS	-3.786	0.103	13.798
PF1434	mbh12 membrane bound hydrogenase alpha (NADHdehydrogenase)	-3.621	0.074	12.309
PF2060	Radical SAM/SPASM domain protein	-3.617	0.107	12.271
PF1432	mbh10 NADH dehydrogenase subunit (like cCoL,EchC, HycH)	-3.448	0.297	10.914
PF0559	hydrogenase expression/formation regulatoryprotein	-3.133	1.347	8.778
PF0892	sulfhydrogenase gamma subunit	-3.052	0.847	8.295
PF1796	putative polyferredoxin	-3.043	0.025	8.242
PF0893	sulfhydrogenase delta subunit	-3.037	0.521	8.21
PF1436	mbh14 iron-sulfur protein (like HycF, EchF,CooX)	-3.023	0.097	8.132
PF1795	sarcosine oxidase subunit alpha	-2.987	0.113	7.928
PF0741	Thioredoxin	-2.678	0.113	6.4
PF0752	thioredoxin peroxidase	-2.538	1.137	5.81
PF1277	7-carboxy-7-deazaguanine synthase	-2.081	0.138	4.233
PF1003	phosphate-binding periplasmic protein precursor(pbp)	-2.005	0.452	4.015
PF1194	transcriptional regulator (furr family)	-1.992	0.172	3.978
PF0894	sulfhydrogenase alpha subunit	-1.98	0.109	3.947
PF0846	Amidohydrolase	-1.95	0.003	3.864
PF0731	copper-transporting atpase, p-type	-1.896	0.296	3.722
PF0602	flavin reductase family protein	-1.866	0.026	3.645
PF0344	tungsten-containing aldehyde ferredoxinoxidoreductase cofactor modifying protein	-1.837	0.142	3.573
PF0345	molybdopterin converting factor, subunit 1	-1.644	0.216	3.126
PF1158	Elp3/Radical SAM protein	-1.626	0.009	3.088
	1	I	1	1

Table S5. Cellular elemental concentrations of samples (μ M). Sulfur measurements for the Δ IssA strain were unreliably low and so are not included. Each measurement is n=1 in which each sample was divided into three aliquots and digested and analyzed independently. The uncertainties are standard deviations for those determinations. Exp, harvested during exponential growth phase; St.St, harvested during stationary growth phase.

Sample	Fe	P	S	Mn	Co	Cu	Zn
WT-S ⁰ (Exp)	1030 ± 10	65500 ± 500	78000 ± 13000	0.065 ± 0.01	7 ± 1	145 ± 1	540 ± 5
WT-S ⁰ (St.St)	660 ± 10	42600 ± 400	40800 ± 800	0.65 ± 0.05	5 ± 1	23 ± 1	510 ± 10
WT+S ⁰ (Exp)	5250 ± 60	45900 ± 700	358600 ± 4400	9 ± 0.5	67 ± 1	305 ± 3	4990 ± 60
WT+S ⁰ (St.St)	8700 ± 300	47100 ± 1500	648000 ± 19000	22 ± 1	115 ± 5	550 ± 20	7400 ± 300
ΔIssA-S ⁰ (Exp)	1300 ± 300	40000 ± 4100	-	1 ± 1	3 ± 1	32 ± 3	150 ± 20
$\Delta IssA+S^{0}(Exp)$	9100 ± 400	78700 ± 1100	1	17 ± 1	44 ± 15	300 ± 50	690 ± 200

Table S6. Strains used in this study

Trivial Name	Strain Name	Description	Ref.	
WT	MW0002	$\Delta pyrF$	59	
ΔIssA	MW0012	$\Delta pyrF \Delta sipA::Pgdh pyrF$	60	